iScience

CellPress
OPEN ACCESS

Article

Myosin 10 Regulates Invasion, Mitosis, and Metabolic Signaling in Glioblastoma

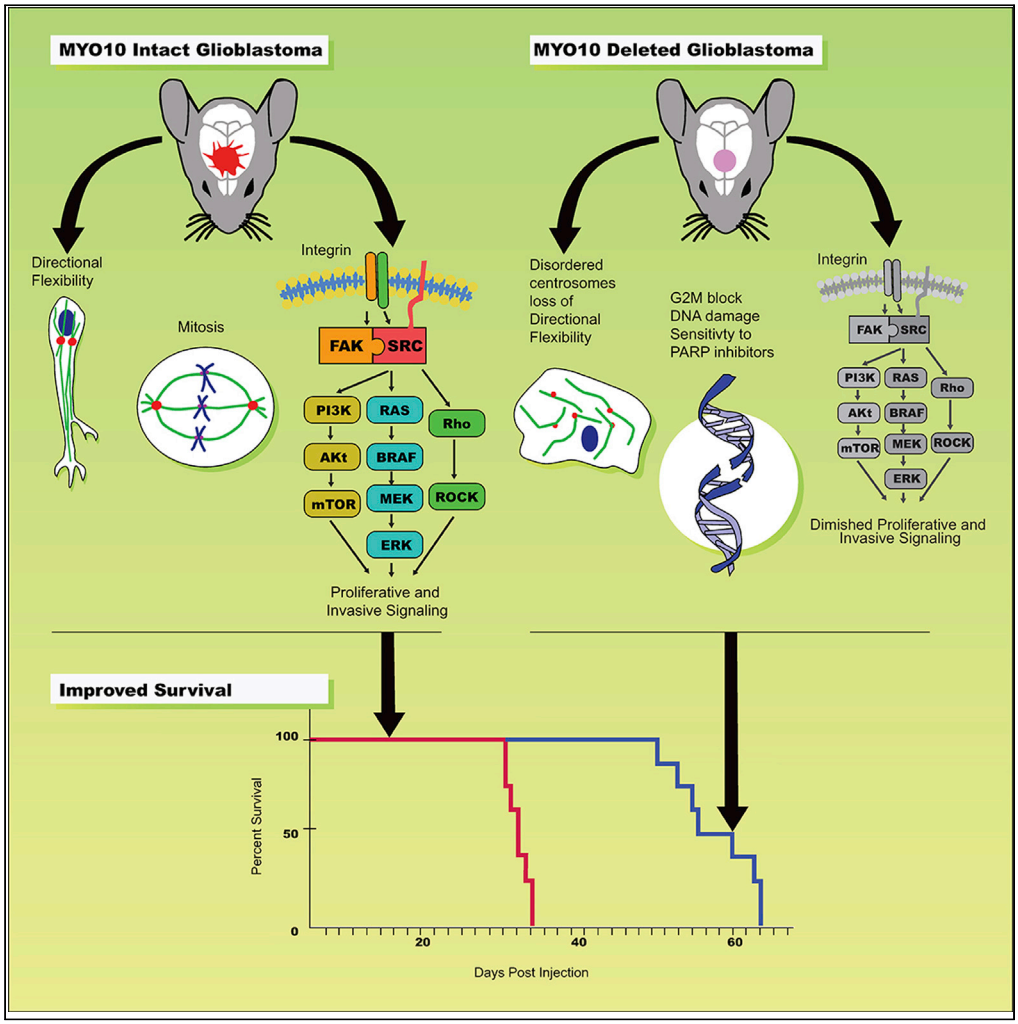

Rajappa S. Kenchappa, Panagiotis Mistriotis, Emily Wisniewski, ..., Konstantinos Konstantopoulos, Peter Canoll, Steven S. Rosenfeld

rosenfeld.steven@mayo.edu

HIGHLIGHTS

Myosin 10 provides glioblastoma cells with directional flexibility

Myosin 10 drives glioblastoma growth by stimulating integrin-dependent signaling

Myosin 10 deletion induces DNA damage and sensitizes tumors to PARP inhibitors

Targeting myosin 10 prolongs survival in mouse models of glioblastoma

Kenchappa et al., iScience 23, 101802
December 18, 2020
https://doi.org/10.1016/j.isci.2020.101802

iScience

CellPress
OPEN ACCESS

Article

Myosin 10 Regulates Invasion, Mitosis, and Metabolic Signaling in Glioblastoma

Rajappa S. Kenchappa,[1] Panagiotis Mistriotis,[2] Emily Wisniewski,[2] Santanu Bhattacharya,[3] Tanmay Kulkarni,[3] Rita West,[1] Amanda Luu,[1] Meghan Conlon,[1] Ernest Heimsath,[4] James F. Crish,[5] Hannah S. Picariello,[5] Athanassios Dovas,[6] Natanael Zarco,[7] Montserrat Lara-Velazquez,[7] Alfredo Quiñones-Hinojosa,[1,7] John A. Hammer,[8] Debrabrata Mukhopadhyay,[3] Richard E. Cheney,[4] Konstantinos Konstantopoulos,[2] Peter Canoll,[6] and Steven S. Rosenfeld[1,7,9,*]

SUMMARY

Invasion and proliferation are defining phenotypes of cancer, and in glioblastoma blocking one stimulates the other, implying that effective therapy must inhibit both, ideally through a single target that is also dispensable for normal tissue function. The molecular motor myosin 10 meets these criteria. Myosin 10 knockout mice can survive to adulthood, implying that normal cells can compensate for its loss; its deletion impairs invasion, slows proliferation, and prolongs survival in murine models of glioblastoma. Myosin 10 deletion also enhances tumor dependency on the DNA damage and the metabolic stress responses and induces synthetic lethality when combined with inhibitors of these processes. Our results thus demonstrate that targeting myosin 10 is active against glioblastoma by itself, synergizes with other clinically available therapeutics, may have acceptable side effects in normal tissues, and has potential as a heretofore unexplored therapeutic approach for this disease.

INTRODUCTION

Glioblastoma (GBM) is among the most common and lethal of primary brain tumors, with a 5-year survival rate that has remained at approximately 5% in spite of decades of clinical investigation (Puduvalli and Hoang, 2018). Two of its defining phenotypes are its ability to proliferate uncontrollably within and to disperse widely throughout the brain (Giese and Westphal, 1996; Burger and Kleihues 1989). Previous studies have demonstrated that GBM cells either proliferate or invade and that inhibiting one stimulates the other (Dhruv et al., 2013; Picariello et al., 2019; Lu et al., 2012; Norden et al., 2008). We had recently shown that whereas targeting the molecular motor non-muscle myosin IIA (NMIIA) markedly impairs GBM invasion, it also accelerates tumor growth (Picariello et al., 2019). These findings led us to hypothesize that effective therapy requires targeting both proliferation and invasion. We had previously shown that targeting both the NMIIA and IIB isoforms together significantly impairs both invasion and proliferation, due to the roles these molecular motors play in mitosis and cell motility, and markedly prolongs survival in genetically engineered mouse models (GEMMs) of GBM (Picariello et al., 2019). Other molecular motors are also involved in both mitosis and motility. Targeting one of these, the kinesin Kif11, blocks GBM proliferation, invasion, and self-renewal (Venere et al., 2015) and prolongs survival in an orthotopic patient-derived xenograft (PDX) model. However, suppression of Kif11 in normal cells leads to mitotic catastrophe and apoptosis. Thus, we propose that a promising GBM target also needs to satisfy two additional criteria. First, it needs to be dispensable for normal cells, as evidenced by the presence of a viable knockout mouse. Second, its targeting should synergize with other therapies, as tumor cells often adapt to loss of one cellular component by activating others (Lathia et al., 2015).

The molecular motor myosin 10 (*MYO10*) meets these criteria. MYO10 is required for cell motility, which drives tumor metastasis (Kerber and Cheney, 2011; Plantard et al., 2010). It is upregulated in lung, prostate, and breast carcinomas; its level of expression in melanoma correlates with metastatic capacity; and its deletion reduces metastases and prolongs survival in a mouse model of melanoma (Bidkhori et al., 2013; Cao et al., 2014; Arjonen et al., 2014; Sun et al., 2015; Makowska et al., 2015; Tokuo et al., 2018). In addition, MYO10 plays a role in mitosis by localizing a variety of mitotic and spindle regulators, including microtubules, TPX2, and Wee1, through the MyTH4/FERM domain in its C-terminal tail (Kwon et al., 2015; Woolner

[1]Department of Cancer Biology, Mayo Clinic, 4500 San Pablo Road, Jacksonville, FL 32224, USA

[2]Department of Chemical and Biomolecular Engineering, Johns Hopkins University, Baltimore, MD 21218, USA

[3]Departments of Biochemistry and Molecular Biology and Physiology and Biomedical Engineering, Mayo Clinic, Jacksonville, FL 32224, USA

[4]Department of Cell Biology and Physiology, and the Lineberger Comprehensive Cancer Center, University of North Carolina, Chapel Hill, NC 27599, USA

[5]Department of Cancer Biology, Lerner Research Institute, Cleveland, OH 44106, USA

[6]Department of Pathology and Cell Biology, Columbia University, New York, NY 10032, USA

[7]Department of Neurosurgery, Mayo Clinic, Jacksonville, FL 32224, USA

[8]Cell and Developmental Biology Center, National Heart Lung and Blood Institute, NIH, Bethesda, MD 20892, USA

[9]Lead Contact

*Correspondence: rosenfeld.steven@mayo.edu

https://doi.org/10.1016/j.isci.2020.101802

et al., 2008; Sandquist et al., 2018). MYO10 also binds several signaling proteins, including β integrins and PKCι (Zhang et al., 2004; Linch et al., 2013). Furthermore, the MYO10 C-terminal tail contains three pleckstrin homology (*PH*) domains that bind signaling phosphatidyl inositols (Plantard et al., 2010; Cox et al., 2002). Finally, although ~50% of MYO10 knockout mice die at or before birth due to severe neural tube closure defects, the remainder are born with only minor defects, grow to adulthood, and breed successfully, implying that otherwise normal cells can compensate for the loss of this motor (Tokuo et al., 2018; Heimsath et al., 2017).

In this study, we have examined the roles MYO10 plays in GBM biology. We show that targeting MYO10 impairs GBM invasion, slows tumor proliferation, reduces integrin-related signaling, and prolongs survival in GEMMs. However, MYO10 deletion also induces GBMs to activate compensatory processes, including the DNA damage and metabolic stress responses, and inhibiting these is synthetically lethal in the face of MYO10 deletion. Thus, while a MYO10 inhibitor for GBM may be therapeutic and relatively non-toxic, it may also synergize with inhibitors of pathways that it modulates through induction of synthetic lethality. These features highlight the potential that MYO10 has as a therapeutic target in GBM.

RESULTS

Deletion of MYO10 Prolongs Survival in Rodent Models of GBM and Impairs Tumor Dispersion *In Vivo*

We queried The Cancer Genome Atlas database for MYO10 expression across GBM subtypes (Figure 1A). Compared with brain (*B*), MYO10 mRNA is upregulated in both the classical (*C*) and proneural (*P*) GBM subtypes (*two-tailed t test*), whereas differences between brain (*B*) and mesenchymal GBM (*M*) are not significant. We also assessed the expression of MYO10 at the protein level in human brain, astrocytoma, and GBM. MYO10 protein expression is approximately 2-fold higher in GBM than in either the astrocytoma or the brain (Figure 1B, *two-tailed t test*).

To determine the importance of MYO10 in driving GBM behavior, we utilized an immunocompetent GEMM that we have previously described (Picariello, et al., 2019). This is illustrated in Figure 1C and involves the injection of a bicistronic retrovirus encoding for a platelet-derived growth factor (PDGF)-hemagglutinnin (HA) fusion protein and the cre recombinase. Intracerebral injection of this virus in mice with floxed alleles for a tumor suppressor (*either PTEN or TP53*) and a gene of interest leads to development of proneural GBMs deleted for PTEN or TP53 and the gene under investigation. In this study, we injected virus into four groups of mice, with floxed alleles for PTEN ± MYO10 and for TP53 ± MYO10. Median survival for mice with TP53-deleted tumors (*TP53(−/−)*; *blue broken curve*) is 32 days post injection (dpi), whereas that for PTEN(−/−) tumors (*blue solid curve*) is > 2-fold longer (79 dpi). However, in both cases, co-deleting MYO10 prolongs median survival—by 9 days in TP53/MYO10(−/−) tumors (*red broken curve*; $p = 0.0002$, *log rank test*) and by 20 days in PTEN/MYO10(−/−) tumors (*red solid curve*; $p = 0.0037$, log rank test) (Figure 1D). We probed primary GBM cell lines from PTEN(−/−) and PTEN/MYO10(−/−) tumors for MYO10 protein expression and compared with RPE1 cells as a positive control (Figure 1E). A band of the expected M_r for MYO10 (*237 kDa*) is seen in both RPE1 and PTEN(−/−) cells (*blue arrow*). However, the PTEN(−/−) cells also express a second band (*red arrow*) with molecular weight consistent with a "headless" MYO10 variant that utilizes an alternative transcription start site and is expressed in nervous system tissue (*163 kDa*) (Raines et al., 2012). Neither is detected in the PTEN/MYO10(−/−) cells.

To determine how MYO10 affects tumor morphology, we generated TP53(−/−) and TP53/MYO10(−/−) tumors and sacrificed animals at the time of tumor morbidity (28 days for *TP53(−/−)* tumors and 40 days for *TP53/MYO10(−/−)* tumors). Brains were excised and histologic sections stained for the HA epitope, to mark PDGF-secreting tumor cells (Ki67, MYO10, and H&E) (Figures 1F–1I). MYO10 deletion results in tumors that are approximately 2-fold smaller in cross-sectional area (Figures S1A and S1B). The regions encompassed by the black rectangle in Figures 1F and 1G are shown at higher magnification in the lower panels and demonstrate less dispersion through the corpus callosum (Figure 1F, *black arrows*) and none through the cortex (Figure 1G, *black arrows*) with MYO10 deletion. TP53(−/−) tumors stain robustly for MYO10 (Figure 1H, *left*), whereas TP53/MYO(−/−) tumors only show MYO10 staining in blood vessels (Figure 1H, *right*, *black arrows*).

MYO10 Deletion Alters GBM Cell Morphology and Mechanics

In PTEN(−/−) cells, MYO10 is distributed in both the nucleus, as previously described (Woolner et al., 2008), and the cytoplasm and membrane ruffles (Figure S2A). MYO10 binds to both actin filaments, through its

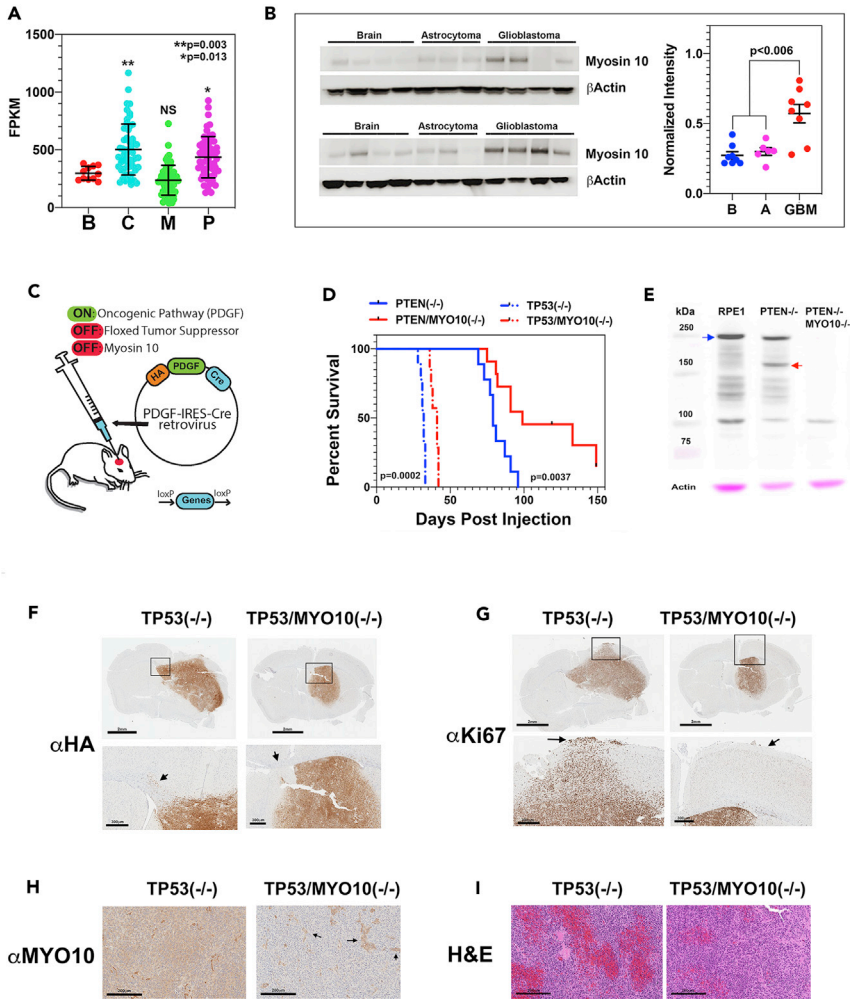

Figure 1. MYO10 Deletion Prolongs Survival in GBM and Reduces Tumor Cell Dispersion *In Vivo*

(A) MYO10 gene expression from The Cancer Genome Atlas database from brain (B) and classical (C), mesenchymal (M), and proneural (P) GBM.

(B) Tumor lysates from human resection specimens of brain (B), astrocytoma (A), and GBM were blotted for MYO10 (*left*) and actin (*right*). Data plotted as mean ± 1 SD.

(C) Illustration of the murine proneural GBM model.

(D) Kaplan-Meier survival curves for mice with TP53- (*blue dashed*), TP53 and MYO10- (*red dashed*), PTEN- (*blue solid*), and PTEN and MYO10 (*red solid*)-deleted tumors (p values derived from log rank test).

(E) Primary tumor cell lines deleted for PTEN or for PTEN and MYO10 were probed for MYO10 expression by western blot. Both RPE1 and PTEN(−/−) cells express the full length MYO10 gene product (*blue arrow*). PTEN(−/−) cells also express a truncated species with the expected M_r for the "headless" isoform of MYO10 (*red arrow*).

(F) Mice with TP53 (*left*) or TP53 and MYO10 (*right*)-deleted tumors were sacrificed at the time of tumor morbidity, brains were excised, and stained for the hemagglutinin (HA) epitope. In the upper images (scale bar, 2 mm), the black rectangles identify images in the bottom panels at higher magnification (scale bar, 500 μm). Black arrows demonstrate that whereas HA-positive cells can be readily found in the corpus callosum of TP53(−/−) tumors, few are seen in TP53/MYO10(−/−) tumors.

(G) Histologic sections from the same location stained for Ki67 (scale bar, 2 mm). Higher-magnification images are displayed in the lower panels (scale bar, 500 μm).

(H) Immunohistochemical stain for MYO10 in TP53(−/−) (*left panel*) and TP53/MYO10(−/−) (*right panel*) tumors. TP53(−/−) tumors stain robustly for MYO10, whereas only tumor blood vessels (black arrows) stain for MYO10 in TP53/MYO10(−/−) tumors.

(I) H&E sections of TP53(−/−) (*left*) and TP53/MYO10(−/−) (*right*) tumors (scale bar, 200 μm).

N-terminal motor domain, and microtubules, through its C-terminal MyTH4/FERM domain, and has been shown to cross-link mitotic spindle microtubules to the surrounding actin cytoskeleton (Kwon et al., 2015) in metaphase. However, loss of this cross-linking function might alter cellular morphology and mechanics in interphase as well. MYO10 deletion flattens GBM cells cultured on fibronectin-coated glass surfaces by 22% and increases spread surface area by nearly 3.5-fold (Figures 2E and 2F). It also redistributes actin into prominent central stress fibers (Figures 2A and 2B), as previously described (Makowska et al., 2015). These findings suggest that MYO10 deletion softens the cytoplasm, as might be expected if this motor were involved in cross-linking the cytoskeleton. To test this hypothesis, we performed atomic force microscopy of MYO-intact and -deleted cells over the cell body. As Figure 2G demonstrates, MYO10 loss is associated with a highly significant decrease in the Young's modulus.

As MYO10 is involved in spindle dynamics (Kwon et al., 2015; Woolner et al., 2008; Sandquist et al., 2018), we stained MYO10-intact and -deleted cells for pericentrin and γ-tubulin to visualize the centrosomes. In PTEN(−/−) cells (Figure 2C), pericentrin and γ-tubulin staining define a punctate, perinuclear structure, consistent with the appearance of centrosomes in interphase. By contrast (Figure 2D), centrosomes appear fragmented in most MYO10-deleted cells. This is also illustrated in Figure S2B at lower magnification, where PTEN(−/−) (*left*) and PTEN/MYO10(−/−) (*right*) cells have been stained for pericentrin (*red*) and α-tubulin (*green*). Although nearly all PTEN(−/−) cells display a discrete red focus, pericentrin staining is more diffuse in approximately 40% PTEN/MYO10(−/−), suggesting that MYO10 deletion induces centrosome disruption or duplication.

MYO10 Deletion Impairs GBM Invasion due to Defects in Cell Directionality

We examined PTEN(−/−) and PTEN/MYO10(−/−) cells for their motility on a 2D barrier-free laminin-coated surface, using a wound assay. Figure 3A reveals that wound closure speed for MYO10-deleted GBM cells ($29.4 \pm 1.4\ \mu m/h$) is nearly identical to that for MYO10-intact cells ($31.0 \pm 1.3\ \mu m/h$). Figure 3B depicts the number of nuclei per 20× field that have extruded through a 3-μm Transwell for PTEN(−/−) (*blue*) versus PTEN/MYO10(−/−) (*red*) cells, whereas Figure 3C depicts the corresponding data for TP53(−/−) (*blue*) and TP53/MYO10-(−/−) (*red*) cells. Although TP53-deleted cells are more invasive than their PTEN-deleted counterparts, in both cases, MYO10 deletion reduces invasion 2.4- to 3.7-fold. We also suppressed MYO10 in four primary human GBM cell lines (GBM1A, L1, GBM162, QNS120) with small hairpin RNA (shRNA) (Figure S3A). Two of these lines (GBM1A and L1) have tumor-initiating cell features (Galli et al., 2004; Deleyrolle et al., 2011). In each case, we also find that suppression of MYO10 significantly impairs Transwell migration (Figure S3B, $p < 0.0001$ by one-way ANOVA). These *in vitro* assays suggest that whereas targeting MYO10 has little effect on cell motility on a barrier-free surface, it appreciably impairs motility when cells need to negotiate through more confined spaces. This is consistent with our histologic examination of MYO10-intact and -deleted GBMs (Figures 1F and 1G), as brain intercellular space is sub-micrometer in size (Thorne and Nicholson, 2006).

However, in addition to being spatially constricted, the pathways through which GBM cells maneuver are also highly non-linear, requiring tumor cells to shift direction when their pathway turns, and to make directional decisions when it branches—a feature we refer to as *directional flexibility*. Centrosomes determine migration directionality for many cells, including astrocytes (Luxton and Gundersen, 2011), and given the effect MYO10 deletion has on centrosome distribution, we wondered if its deletion affected directional flexibility. We therefore utilized microfabricated *in vitro* invasion assays, which have been described previously (Zhao et al., 2019; Mistriotis et al., 2019). We first examined PTEN(−/−) and PTEN/MYO10(−/−) cell motility through fibronectin-coated straight channels with a constant height ($H = 10\ \mu m$) and varying width ($W = 10, 6,$ or $3\ \mu m$). Although both types of cells migrated with similar speeds through these channels (Figure 3D), PTEN/MYO10(−/−) cells migrated with significantly higher directional persistence (Figure 3E and Video S1). To examine this further, we studied the migration behavior of these cells when they encountered a trifurcating microchannel (Figure 3F). In this configuration, cells first migrate through a 200-μm-long feeder channel before reaching a trifurcation, where they face a decision about which direction to turn. The dimensions of the three branched channels are distinct, although the hydraulic resistance of each branch is constant. We found that a higher percentage of PTEN/MYO10(−/−) cells were able to reach the trifurcation (Figure 3G and Video S2) due to their increased directional persistence. Although PTEN(−/−) and PTEN/MYO10(−/−) cells displayed a similar ability to make the decision to migrate through one of the three branched channels (Figure 3H), PTEN/MYO10(−/−) cells took significantly longer to decide which direction to turn (Figure 3I). Furthermore, the highest fraction of PTEN(−/−) cells migrated

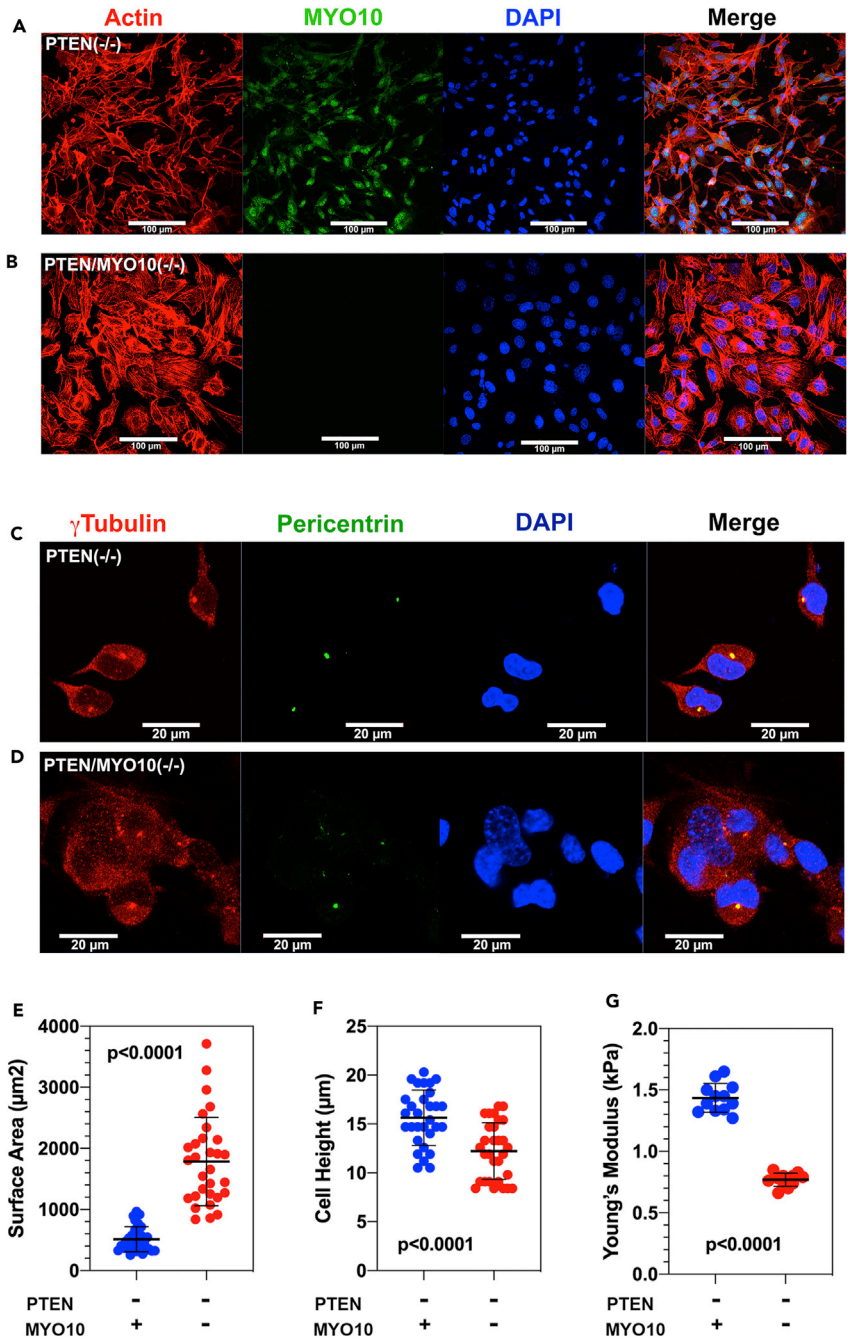

Figure 2. MYO10 Deletion Alters GBM Cell Morphology and Mechanics

(A and B) PTEN(−/−) (A) and PTEN/MYO10(−/−) (B) cells were grown on coverslips and stained for actin, MYO10, and DAPI. Scale bars, 100 µm.

(C and D) PTEN(−/−) (C) and PTEN/MYO10(−/−) (D) cells were stained for γ-tubulin, pericentrin, and DAPI. Scale bars, 20 µm.

(E) Surface area for GFP-expressing PTEN(−/−) (*blue*) and PTEN/MYO10(−/−) (*red*) cells plated on glass bottom dishes coated with fibronectin.

(F) Cell height for GFP-expressing PTEN(−/−) (*blue*) and PTEN/MYO10(−/−) (*red*) cells.

(G) Young's modulus for PTEN(−/−) (*blue*) and PTEN/MYO10(−/−) (*red*) cells measured over the cell body. Error bars depict mean ± 1 SD.

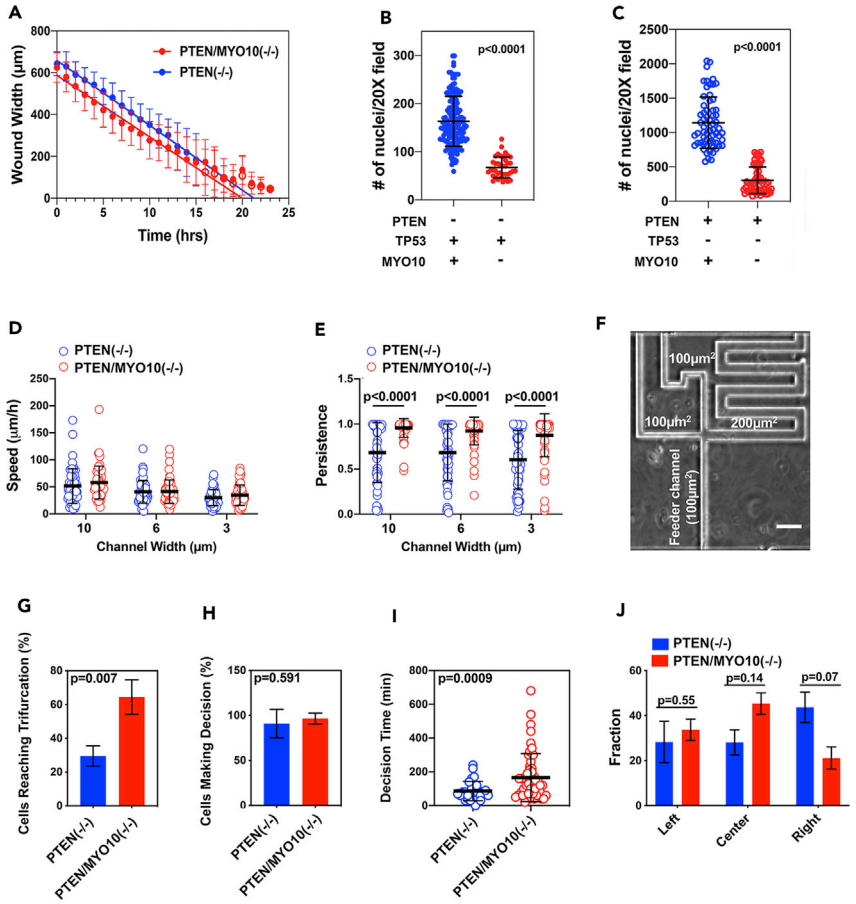

Figure 3. MYO10 Deletion Reduces GBM Invasion through Confined Spaces by Affecting Directional Persistence

(A) Cell velocities in an *in vitro* wound assay for PTEN(−/−) (*blue*) and PTEN/MYO10(−/−) (*red*) cells.

(B) Migration over 12 h through a 3-μm Transwell chamber was measured for PTEN(−/−) (*blue*) and PTEN/MYO10(−/−) (*red*) cells.

(C) Corresponding Transwell assay for TP53(−/−) (*blue*) and TP53/MYO10(−/−) (*red*) cells.

(D and E) Cell migration speed (D) and persistence (E) of PTEN(−/−) (*blue*) and PTEN/MYO10(−/−) (*red*) cells in 10-μm-high × 10-, 6-, or 3-μm-wide fibronectin-coated microchannels.

(F) Image of a trifurcating microchannel.

(G) Percentage of PTEN(−/−) (*blue*) and PTEN/MYO10(−/−) (*red*) cells able to migrate through the 200-μm-long feeder channel to the trifurcation over a period of 24 h.

(H) Percentage of PTEN(−/−) (*blue*) and PTEN/MYO10(−/−) (*red*) cells that made a decision to migrate through one of the three branched channels after reaching the trifurcation over a period of 24 h. Cells that did not make a decision either reversed direction or remained stuck in the trifurcation until the end of the imaging period.

(I) Time required for PTEN(−/−) (*blue*) and PTEN/MYO10(−/−) (*red*) cells to make a decision to migrate through one of the three branched channels after the cell body reached the trifurcation.

(J) Fraction of PTEN(−/−) (*blue*) and PTEN/MYO10(−/−) (*red*) cells migrating through the left, center, or right branch after reaching the trifurcation (*n = 3 independent experiments*). Data represent mean ± SD (D, E, and I) or mean ± SEM (G, H, and J).

through the right-most channel, which has the largest cross-sectional area of the three branches (Figure 3J). By contrast, the highest fraction of PTEN/MYO10(−/−) migrated through the center branch, suggesting that these cells prefer to maintain direction rather than travel along a wider track.

MYO10 Deletion Slows Tumor Proliferation

We measured tumor cell doubling time in an environmentally controlled live-cell imaging microscope (Figure 4A). Doubling time for PTEN(−/−) cells (*15.9 ± 5.2 h*) is ~66% shorter than that for PTEN/MYO10(−/−) cells (*24.4 ± 7.6 h*) on a glass surface ($p < 0.0001$, two-tailed t test). However, tumor tissue is considerably

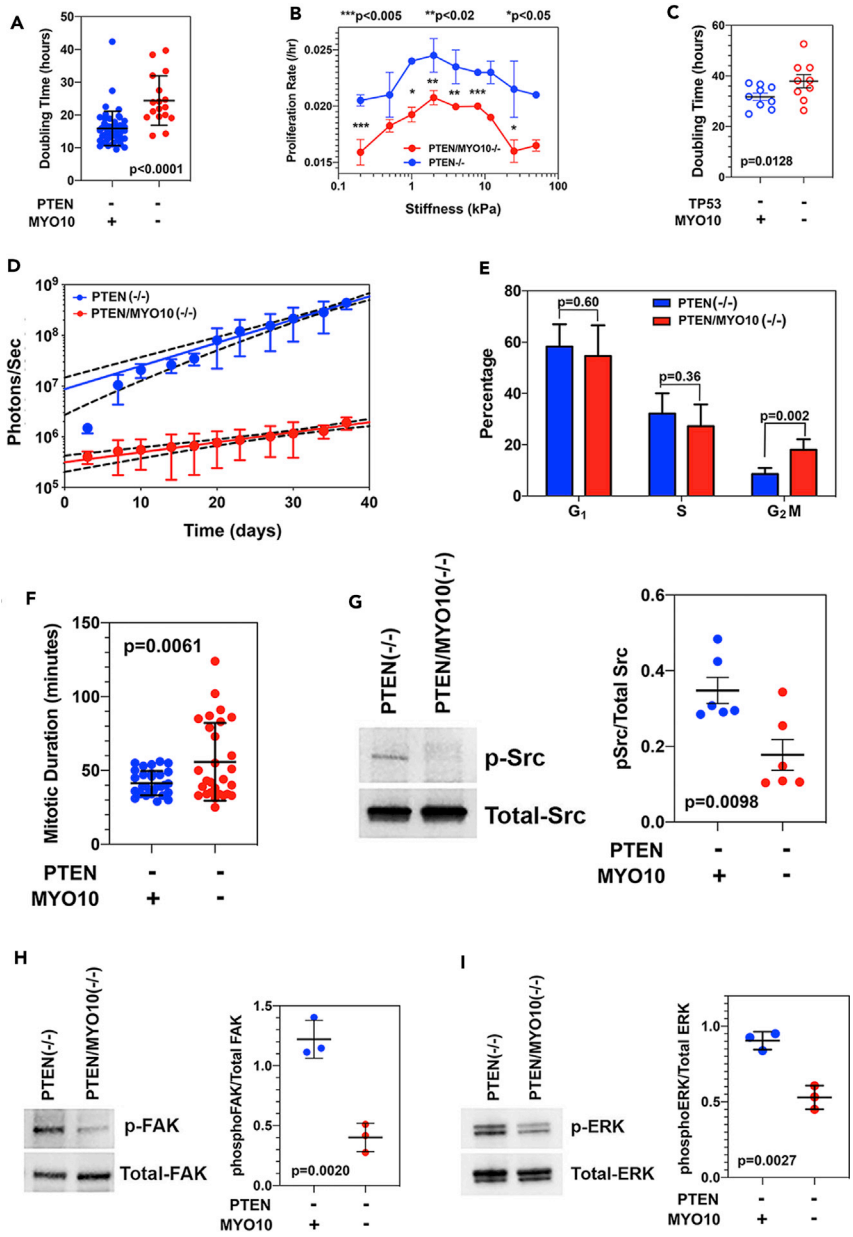

Figure 4. MYO10 Deletion Slows Tumor Cell Proliferation and Reduces Integrin-Related Signaling

(A) Doubling time for PTEN(−/−) (*solid blue*) and PTEN/MYO10(−/−) (*solid red*) cells monitored in an environmentally controlled microscope for 4 days.

(B) Growth rates were measured for PTEN(−/−) (*solid blue*) and PTEN/MYO10(−/−) (*solid red*) cells grown on fibronectin-derivatized hydrogels of defined stiffness (*Softwells*, *Matrigen*). Cell count was measured every 12 h for 4 days, and data were fit to an exponential growth equation to yield proliferation rates (h^{-1}).

(C) Growth rates of TP53(−/−) (*open blue*) and TP53/MYO10(−/−) (*open red*) cells on tissue culture plastic.

(D) 50,000 luciferase-expressing PTEN(−/−) and PTEN/MYO10(−/−) cells were injected into the white matter of NSG recipient mice, and tumor growth was measured using bioluminescence. Luminescence over time was fit to single exponential growth equations (*solid colored lines with 95% CI indicated by black dashed lines*).

(E) PTEN(−/−) (*solid blue*) and PTEN/MYO10(−/−) (*solid red*) cells were stained with DAPI and examined by flow cytometry. MYO10 deletion leads to a greater than 2-fold increase in the fraction of cells in G_2M ($p = 0.002$, two-tailed t test).

(F) Duration in M phase was measured by time lapse microscopy of PTEN(−/−) (*solid blue*) and PTEN/MYO10(−/−) (*solid red*) cells in an environmentally controlled microscope for 4 days.

Figure 4. *Continued*
(G–I) Phosphorylation of SRC (G), FAK (H), and ERK1/2 (I) was measured by western blot (*left panels*), and the ratio of phosphorylated/total species (*right panel*) is reduced in PTEN/MYO10(−/−) tumor cells (*solid red*) compared with PTEN(−/−) tumor cells (*solid blue*) in each case. Error bars represent mean ± 1 SD.

softer than tissue culture plastic or glass, and as we demonstrated in our recent study, GBM growth rate varies with substrate stiffness (Picariello et al., 2019). We therefore cultured PTEN(−/−) (*solid blue*) and PTEN/MYO10(−/−) (*solid red*) cells on fibronectin-coated hydrogels with defined stiffnesses ranging from 0.2 to 50 kPa (*Matrigen, Brea, CA*). As Figure 4B shows, PTEN(−/−) cells show an optimum for growth on surfaces with Young's modulus from ~1 to 10 kPa. Although MYO10 deletion slows the proliferation rate 25%–30% across the entire range of stiffness, the stiffness optimum does not change. We also measured proliferation kinetics of GBM cells deleted for TP53 or co-deleted for TP53 and MYO10 on tissue culture plastic (Figure 4C) and find the same pattern as in Figure 4A—longer doubling time with MYO10 deletion. shRNA suppression of MYO10 in the four human GBM lines grown on tissue culture plastic also slows proliferation, and to a degree similar to what we observe with our murine GBMs (Figure S3C).

As the microenvironments that constitute a GBM tumor have features not replicated by *in vitro* experimental platforms, we injected 50,000 luciferase-expressing PTEN(−/−) and PTEN/MYO10(−/−) into the white matter of NSG mice, and monitored tumor growth with bioluminescence. Results are depicted in Figure 4D for PTEN(−/−) cells (*solid blue*) and PTEN/MYO10(−/−) cells (*solid red*). The slopes of the fits define *in vivo* doubling times of 6.6 ± 1.2 days for PTEN(−/−) cells and 15.3 ± 4.4 days for PTEN/MYO10(−/−) cells. These are considerably longer than the corresponding *in vitro* values (Figures 4A and 4B) and presumably reflect differences in environmental factors that modulate growth. However, the overall pattern remains the same—MYO10 deletion slows tumor proliferation.

As one of the functions of MYO10 is in positioning the mitotic spindle, we might expect that its deletion could alter progression through M phase. Flow cytometry of DAPI-stained PTEN(−/−) and PTEN/MYO10(−/−) tumor cells (Figure 4E, *blue versus red*) confirms that MYO10 deletion enhances accumulation in G_2M. This implies that mitotic duration is prolonged with MYO10 deletion, and we tested this in a live-cell imaging microscope by measuring the time between initial cell rounding and cytokinesis. This increases from 41.4 ± 8.3 to 55.9 ± 26.3 min with MYO10 deletion (Figure 4F, $p = 0.0061$, two-tailed t test). Although consistent with its role in spindle function, this 35% increase in M phase duration does not explain the 8.5-h difference in cell doubling time, and suggests that other factors contribute as well to the slower growth of MYO10-deleted tumors. MYO10 regulates signaling through its interaction with β-integrins (Arjonen et al., 2014; Zhang et al., 2004; Miihkinen et al., 2020). Integrins activate SRC, focal adhesion kinase (FAK), and the Ras-Raf-MEK-ERK pathway, and each in turn can stimulate invasion and proliferation. In each case, MYO10 deletion reduces activated levels of these signaling effectors by ≥ 2-fold (Figures 4G–4I).

MYO10 Deletion Enhances the DNA Damage Response and Sensitizes GBMs to a PARP Inhibitor

Delays in mitotic progression lead to DNA damage (Bakhoum et al., 2017), so we probed MYO10-deleted and intact murine GBM cells for PARP, cleaved PARP (Figure S4A), and γH2Ax (Figure S4B). Figures 5A–5C show that MYO10 deletion increases the expression of each 3- to 5-fold. We also observe an increase in γH2Ax in each of the four human GBM cell lines suppressed for MYO10 with shRNA (Figure S4C). This implies that MYO10 deletion increases tumor cell dependence on DNA repair mechanisms, which would predict enhanced sensitivity to inhibitors of the DNA damage response. We measured the dose response for MYO10-intact and -deleted murine tumor cells to the central nervous system-permeant PARP inhibitor niraparib. Dose-response curves (Figures 5D and 5E) show that loss of MYO10 significantly enhances sensitivity to this drug. Likewise, the four human GBM cell lines suppressed for MYO10 also show a >25-fold increased sensitivity to niraparib *in vitro* (Figure S4D).

To test the translational value of these findings, we injected luciferase-expressing PTEN(−/−) and PTEN/MYO10(−/−) cells orthotopically into NSG mice and monitored tumor growth with bioluminescence over time with administration of vehicle or niraparib. We initiated treatment with drug or vehicle when photon counts were between 2.5 and 5.0 × 10^7/s. Results are illustrated in Figure 5F. MYO10-deleted tumors in vehicle-treated mice (*red solid circles*) grow 2–4 times more slowly than do tumors intact for MYO10 (*blue solid circles*), consistent with Figure 4D. Niraparib does not alter growth kinetics of MYO10-intact GBMs (*blue open boxes*), whereas it appreciably slows growth when MYO10 is deleted (*red open boxes*). We next injected our bicistronic

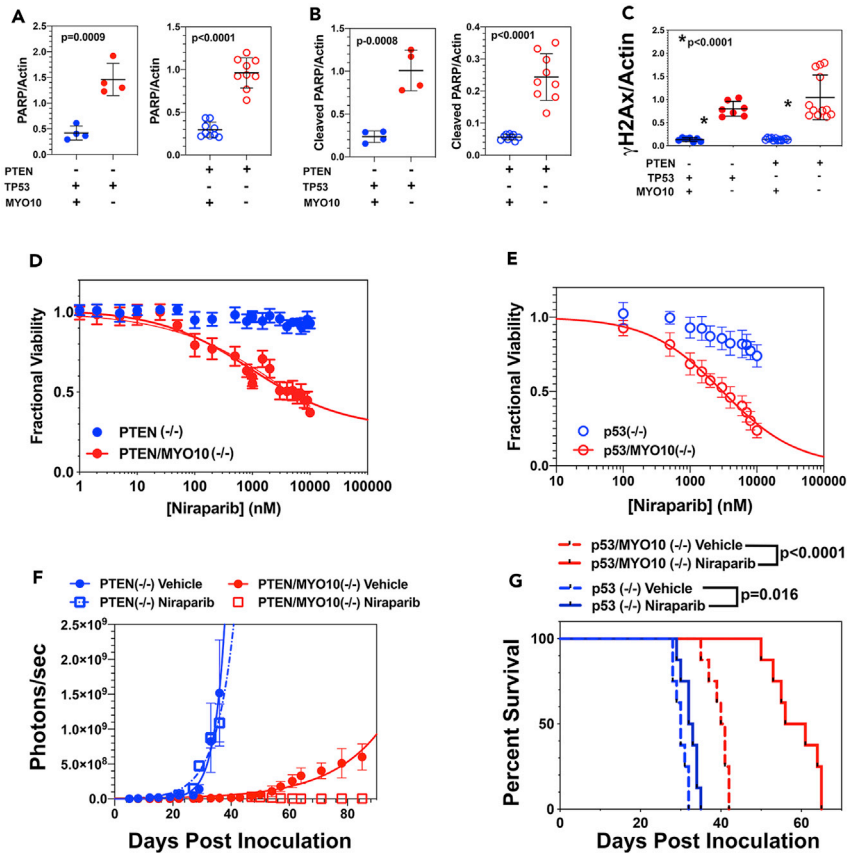

Figure 5. MYO10 Deletion Increases DNA Damage and Sensitizes Tumor Cells to a PARP Inhibitor

(A) Normalized PARP levels for PTEN(−/−) and PTEN/MYO10(−/−) cells (*left panel*) and TP53(−/−) and TP53/MYO10(−/−) cells (*right panel*).

(B) Corresponding plots of cleaved PARP.

(C) MYO10 deletion increases γH2Ax in both PTEN and TP53-deleted backgrounds. Error bars in (A–C) represent mean ± 1 SD.

(D) Dose response of PTEN(−/−) (*solid blue*) and PTEN/MYO10(−/−) (*solid red*) cells to the central nervous system-permeant PARP inhibitor niraparib after 72 h of exposure to vehicle or drug. Data for PTEN/MYO10(−/−) cells fit a Hill equation, yielding values of EC_{50} and Hill coefficient of 4,417 ± 468 nM and 0.43 ± 0.04, respectively.

(E) Corresponding dose-response curves of TP53(−/−) and TP53/MYO10(−/−) cells to niraparib. Data for TP53/MYO10(−/−) cells fit a Hill equation with EC_{50} and Hill coefficient of 3,065 ± 144 nM and 0.79 ± 0.05, respectively.

(F) 50,000 luciferase-expressing PTEN(−/−) and PTEN/MYO10(−/−) cells were orthotopically injected into NSG mice, and tumor growth was monitored with bioluminescence. Once photon counts were between 2.5 and 5.0 × 10^7/s, animals were treated with vehicle (*solid circles*) or niraparib (*open boxes*) at a dose of 25 mg/kg at a frequency of 5 days/week by intraperitoneal injection.

(G) Mice with floxed alleles for TP53 (*blue*) or TP53 and MYO10 (*red*) were injected with PDGF-IRES-cre retrovirus. At 5 days post retroviral injection, animals were treated with 5 days/week dosing of vehicle (*dashed curve*) or niraparib (*solid curve*) at a dose of 25 mg/kg 5 days per week and treatment continued until tumor morbidity. p values derived from log rank tests.

PDGF-IRES-cre retrovirus into mice with floxed alleles for either TP53 or TP53 and MYO10 to generate tumors deleted for these genes. We treated mice with either vehicle ($n = 8$) or niraparib ($n = 8$) until they developed signs of tumor morbidity. Although niraparib prolongs median survival in mice with TP53(−/−) tumors, the effect is very modest (Figure 5G; *blue, solid versus dashed*; *2.5 days = 8%*, $p = 0.016$, *log rank test*). By contrast, niraparib significantly prolongs median survival in mice whose tumors are co-deleted for MYO10 (Figure 5G; *red solid versus dashed*; *18 days = 45% increase in median survival*, $p < 0.0001$, *log rank test*).

What is not clear from the above is whether MYO10 deletion by itself is sufficient to induce DNA damage, or whether this only occurs in the context of malignancy. This issue is translationally relevant, because if MYO10

deletion alone is sufficient, combining a MYO10 inhibitor with a PARP inhibitor or with radiation might be unacceptably toxic to normal tissues. To examine this, we measured PARP (Figure S4E) and γH2Ax (Figure S4F) in lung, spleen, testis, liver, and cerebellum in wild-type (WT), MYO10 heterozygous knockout (HT) mice, and MYO10 homozygous knockout mice (KO). We see no difference between HT and KO mice in PARP for cerebellum, liver, lung, and spleen, with increased PARP expression (but no cleaved PARP) in testes from KO mice. We could not detect γH2Ax expression in any of these tissues from WT, HT, or KO mice, with readily detectable γH2Ax in our positive control (PTEN/MYO10(−/−) tumor cells).

MYO10 Deletion Upregulates the Metabolic Stress Response in a Context-Dependent Manner

To obtain an unsupervised overview of how GBM cells respond to MYO10 deletion, we analyzed lysates of PTEN(−/−) and PTEN/MYO10(−/−) cells with a phospho-antibody array (*Cancer Signaling Phospho-Array, Full Moon Biosystems, Mendeley Data "Myosin 10 Phospho Antibody Array," Mendeley Data, V1, https://doi.org/10.17632/5cnvmf9m2d.1*). Of 135 phosphorylated signaling molecules, we observed only five whose phosphorylation increased ≥70% with MYO10 deletion, and each is connected to metabolic and/or endoplasmic reticulum (ER) stress responses. These include STAT4 (*2.1-fold, pY693*), AMP-activated protein kinase (*AMPK, 1.9-fold, pT183*), HSP90B (*1.8 fold, pS254*); JunB (*1.8-fold, pS259*), JunD (*1.7 fold, pS255*), and caveolin-1 (*1.7-fold, pY14*). The activity of AMPK, a master metabolic regulator is increased >100-fold through phosphorylation of T183 by LKB1 and CAMKII (Hardie 2015). AMPK stimulates pinocytosis and increases the glucose and amino acid uptake (Towler and Hardie, 2007; Bae et al., 2011). We validated our results by performing western blots of total and phospho-AMPK on tumor cell lysates. Representative western blots (Figures S5A and S5B) and quantitation of phospho-AMPK/total AMPK (Figure 6A) reveal that in a PTEN-deleted background, MYO10 co-deletion enhances AMPK phosphorylation ~3-fold, associated with an increase in LKB1 expression but without change in total AMPK (Figures S5C and S5D; Figures 6B and 6C). Loss of MYO10 also enhances activating phosphorylation of AKT by ~3-fold (Figures S5E and 6D). The increased activation of AMPK in PTEN/MYO10-co-deleted cells suggests that these cells are more dependent on AMPK and may be more sensitive to the AMPK inhibitor dorsomorphin. PTEN(−/−) cells are completely resistant, whereas PTEN/MYO10(−/−) cells are sensitive (Figure 6E), with an EC_{50} of 2010 ± 314 nM. To ensure that the effects seen with MYO10 deletion are truly due to the loss of this motor, we suppressed MYO10 expression in PTEN(−/−) cells using stable transfection with two MYO10-directed shRNA-encoding vectors or with a non-targeting (*NT*) control vector. As with genetic deletion, suppression of MYO10 in murine GBM cells increases AMPK phosphorylation and expression of γH2Ax 3- to 4-fold relative to the non-targeting (NT) control (Figure S6).

However, MYO10 does not regulate AMPK and AKT in a TP53-deleted background (Figures 6A and 6D). Both LKB1 and CAMKII are in turn activated by a rise in cytosolic calcium—LKB1 by binding to MO25, a calcium-binding allosteric modifier, and CAMKII by calcium binding to calmodulin. The rise in calcium requires the generation of phosphatidylinositol 3,4,5-trisphosphate (*PIP3)* produced by the action of PI3 Kinase (*PI3K*). AKT is also activated by binding PIP3 through its PH domain (Frech et al., 1997). Hence, the signaling activity of PIP3 could be controlled by two processes—PIP3 dephosphorylation by PTEN and PIP3 sequestration by PH-domain-containing proteins, including MYO10. This suggests that the increase in AMPK and AKT activity we observe requires the combined effects of deleting both PTEN, to enhance PIP3 levels, and MYO10, to reduce PIP3 sequestration. If correct, we would predict that expression of a biologically active PH domain in PTEN/MYO10(−/−) cells would reduce AMPK phosphorylation. As PI3K generates PIP3, we also predict that inhibiting this kinase should also reduce AMPK phosphorylation in PTEN/MYO10(−/−) cells. Furthermore, if co-deletion of PTEN and MYO10 increases bioavailable PIP3, PTEN/MYO10(−/−) tumor cells should have increased dependence on PIP3, and be selectively killed with a PI3K inhibitor. Treatment of PTEN(−/−) cells with the PI3K inhibitor idelalisib (*100 nM*) has no effect on AMPK phosphorylation, suggesting that baseline AMPK phosphorylation is relatively independent of PIP3 availability. However, it does reduce AMPK phosphorylation in PTEN/MYO10(−/−) cells (Figures S4G and 6F). Furthermore, whereas this drug is selectively toxic to PTEN/MYO10(−/−) cells, it has no appreciable effect on PTEN(−/−), TP53(−/−), or TP53/MYO10(−/−) cells (Figure 6G). Finally, we transfected PTEN(−/−) and PTEN/MYO10(−/−) cells with expression plasmids encoding either a PH domain from Bruton tyrosine kinase fused to GFP or GFP as a control. Western blots show that the PH-GFP fusion, but not GFP, restores phospho-AMPK levels (Figures S7A–S7D) but does not alter the increase in γH2Ax levels, which we observed from MYO10 deletion (Figures S7B and S7D), implying that other domains of the MYO10 molecule are needed instead or as well to prevent DNA damage. By contrast, transfection of a full-length MYO10-GFP fusion protein reverses both the increase in phosphorylated AMPK and γH2Ax (Figures S7E–S7H).

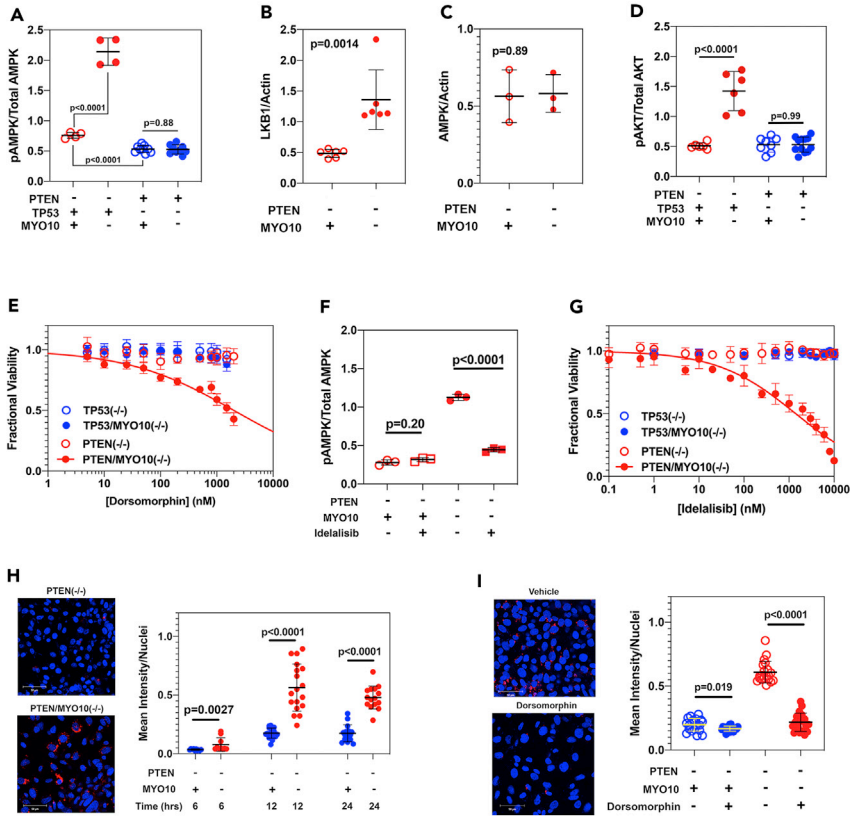

Figure 6. MYO10 Deletion Activates AMPK and AKT and Sensitizes Tumor Cells to AMPK and PI3K Inhibitors

(A) MYO10-deletion increases AMPK-activating phosphorylation (pT 172/183) ~3-fold in a PTEN-deleted background ($p < 0.0001$, two-tailed t test), but not in a TP53-deleted background ($p < 0.0001$, two-tailed t test). Baseline AMPK levels are higher in PTEN(−/−) cells than in TP53(−/−) cells (*open red versus open blue*; $p < 0.0001$, two-tailed t test).

(B) Levels of LKB1 are increased ~3-fold in PTEN-deleted cells with MYO10 co-deletion.

(C) Levels of AMPK are not appreciably altered by MYO10 co-deletion in a PTEN-deleted background ($p = 0.89$, two-tailed t test).

(D) Deletion of MYO10 in cells with a PTEN-deleted background increases AKT phosphorylation ~3-fold ($p < 0.0001$, two-tailed t test), whereas MYO10 deletion in a TP53-deleted background does not ($p = 0.99$).

(E) GBM cells were treated for 72 h with the AMPK inhibitor dorsomorphin. Only PTEN/MYO10(−/−) cells are sensitive to the drug, with EC_{50} and Hill coefficient of 2,010 ± 314 nM and 0.5 ± 0.1, respectively.

(F) PTEN(−/−) cells (*open red*) and PTEN/MYO10(−/−) cells (*closed red*) were treated with 100 nM of the PI3K inhibitor idelalisib for 24 h. Idelalisib has no effect on AMPK phosphorylation in MYO10-intact cells, but reduces it in MYO10-deleted cells.

(G) Dose response to idelalisib for PTEN(−/−) (*open red*), PTEN/MYO10(−/−) (*closed red*), TP53(−/−) (*open blue*), and TP53/MYO10(−/−) (*closed blue*) cells. Only the PTEN/MYO10(−/−) cells show any sensitivity, with an EC_{50} and Hill coefficient of 1,405 ± 182 nM and 0.50 ± 0.05, respectively.

(H) *Left panels*: PTEN(−/−) (*top*) and PTEN/MYO10(−/−) (*bottom*) cells were plated on fibronectin-coated chamber slides and rhodamine-labeled dextran was added. Cells were incubated for 6, 12, and 24 h; fixed; and counterstained with DAPI. Fluorescent imaging after 12 h demonstrates readily detectable red fluorescence in the MYO10-deleted cells with little in MYO10-intact cells. *Right panel*: intensity of red fluorescence in the field divided by the number of DAPI nuclei is plotted for 6, 12, and 24 h for PTEN(−/−) (*blue*) and PTEN/MYO10(−/−) (*red*) cells.

(I) *Left panel*: Fluorescence imaging of PTEN/MYO10(−/−) cells treated for 12 h with rhodamine dextran in the presence of vehicle (*upper panel*) or 200 nM dorsomorphin (*lower panel*). *Right panel*: intensity of red fluorescence in the field divided by the number of DAPI nuclei is plotted for 12 h of exposure to rhodamine dextran for PTEN(−/−) (*blue*) and PTEN/MYO10(−/−) (*red*) cells in the presence of vehicle (*open circles*) or dorsomorphin (*closed circles*). Error bars depict mean ± 1 SD. p values determined from two-tailed t test.

We tested for the effect of MYO10 deletion on AMPK-activated pinocytosis (Towler and Hardie, 2007; Meley et al., 2006) by incubating PTEN(−/−) and PTEN/MYO10(−/−) cells with rhodamine-labeled dextran (M_r *10,000*) for 6, 12, and 24 h and measuring rhodamine fluorescence intensity normalized to the total number of DAPI-stained nuclei (Figure 6H). Examples of images taken at 12 h are illustrated in the left two panels, and normalized intensity at 6, 12, and 24 h for 15 fields is depicted in the right panel. Fluorescence intensity in PTEN/MYO10(−/−) cells remained significantly greater than in PTEN(−/−) cells at each time point (*two tailed t test*), implying that MYO10 deletion enhances rhodamine dextran pinocytosis. We incubated PTEN(−/−) and PTEN/MYO10(−/−) for 12 h with rhodamine dextran in the presence or absence of 200 nM dorsomorphin. Dorsomorphin has little effect in PTEN(−/−) cells, whereas it abolishes the increase in rhodamine dextran uptake induced with MYO10 deletion (Figure 6I).

DISCUSSION

MYO10 Supports the Malignant Phenotype of GBM in Multiple Ways

Given the importance of cell motility in metastasis, it is not surprising that studies of MYO10 in cancer have largely focused on its role in driving tumor invasion. MYO10 has been shown to be important in metastasis in models of malignant melanoma and lung carcinoma (Tokuo et al., 2018; Summerbell et al., 2020). These findings are consistent with the roles MYO10 plays in driving filopodia formation and in activating integrins (Arjonen, et al., 2011; Arjonen, et al., 2014; Zhang et al., 2004; Miihkinen et al., 2020). In lung carcinoma, MYO10 drives collective cell migration, where its expression in leader cells is needed for filopodial persistence and patterning of the extracellular matrix (Summerbell et al., 2020). Collective cell migration in the perivascular space has also been described in some pre-clinical models of GBM, whereas in others, including in our PDGF-driven murine GBM models (Figure 1C), single-cell motility predominates, particularly in white matter (Assanah et al., 2006). Thus, the roles MYO10 plays in tumor biology may vary with both the tumor and the microenvironment. In support of this, while small interfering RNA suppression of MYO10 in lung carcinoma leader cells reduces migration on a 2D surface (Summerbell et al., 2020), its deletion in our murine models of GBM has more subtle effects that are not seen in spatially unconstrained environments (Figure 3A). Rather, MYO10 deletion impairs GBM directional flexibility (Figures 3D–3J). This may explain why we observe significant defects in Transwell migration (Figures 3B and 3C), as tumor cells would need to change direction by 90° to enter the 3-μm pores of the Transwell membrane and crawl through. Loss of directional flexibility would be particularly problematic for tumor cells crawling through the highly branched pathways that they would encounter in brain white matter, cortex, and perivascular space (Assanah et al., 2006). In cell motility, directionality is shaped by actin polymerization in the periphery and centrosome-driven microtubule nucleation, and MYO10 deletion alters the distribution of both (Figures 2A and 2B). This might be mechanistically connected to a loss of MYO10-dependent microtubule-actin cross-linking, which could also explain the cytoplasmic softening that we observe with this motor's deletion (Figure 2G).

MYO10 binds to actin through its motor domain and to microtubules through its C-terminal MyTH4/FERM domain, and as such is able to position the mitotic spindle, containing the centrosomes, by cross-linking spindle microtubules to the actin cortex (Kwon et al., 2015; Woolner et al., 2008). Loss of these functions with MYO10 deletion can explain the lengthening of doubling time and the increase in G_2M fraction (Figure 4E)—features that suggest a dysregulation in the mitotic process. Furthermore, MYO10 deletion inhibits activation of proliferation-stimulating signaling effectors downstream of integrins, including SRC, FAK, and ERK1/2 (Figures 4G–4I). We propose that these combined effects on mitosis and signaling explain the reduced proliferation for MYO10-deleted GBM cells, and together with the impairment in tumor cell motility and invasion, also explain the improvement in survival in tumor-bearing mice (Figure 1D).

Targeting MYO10 Synergizes with Other GBM Therapeutics

Given the roles MYO10 plays in signaling and mitosis and given the importance of these processes to cancer development, it is not surprising that targeting MYO10 alters both, and in ways that are translationally relevant. MYO10 deletion or suppression enhances the DNA damage response in murine and human GBM cells, but not in non-transformed tissues. This suggests that targeting MYO10 can induce DNA damage, but only when it occurs in the background of the genetic instability and/or increased mitotic drive that characterizes tumor cells. Regardless of the underlying mechanisms, this upregulation and activation of the DNA damage response led us to predict that MYO10 deletion would enhance sensitivity to PARP inhibitors, and we have confirmed this. These findings are reminiscent of what is seen in GBM tumor-initiating cells, whose radio- and chemo-resistance have also been attributed to an enhanced DNA damage response (Lathia et al., 2015; Bao et al., 2006). Like MYO10-deleted cells, tumor-initiating cells also have an increased dependence on PARP and respond to treatment with PARP inhibitors (Venere et al., 2014). Our results suggest that systemic targeting of MYO10 through a

small molecule inhibitor may also synergize with other DNA damaging agents, such as radiotherapy or alkylating chemotherapy. Furthermore, we anticipate that this may occur without untoward toxicity to normal cells, as we do not see an increase in DNA damage in non-transformed tissues that are deleted for MYO10.

Deleting or shRNA suppressing MYO10 induces DNA damage across a broad spectrum of GBMs, including both murine tumors deleted for either TP53 or PTEN and four primary human GBM lines, two of which have tumor-initiating cell characteristics (Figures 5 and S4). We can only reverse this effect by replacing with full length MYO10, as opposed to just a PH domain. This implies that should a small molecule inhibitor of the MYO10 motor domain be developed, it should be effective in inducing DNA damage across a variety of GBMs. However, another signaling consequence of MYO10 deletion—activation of AMPK and AKT—appears to specifically require co-deletion of the tumor suppressor PTEN (Figures 6 and S5–S7). Unlike the effect of MYO10 deletion on DNA damage, upregulation of AMPK and AKT activation can be reversed by over-expression of an exogenous PH domain, consistent with our hypothesis that one of the signaling functions of MYO10 is in regulating bioavailable PIP3. This finding is relevant to the human disease, as PTEN mutations are seen in approximately 35% of GBMs (Yang et al., 2017). Our explanation that MYO10 regulates locally generated PIP3 by sequestering it through its PH domains is consistent with studies in mouse hippocampal neurons, which have shown that like MYO10, PIP3 accumulates in filopodia (Luikart et al., 2008).

MYO10 Has Potential as an Unexplored, Therapeutic Target in GBM

Members of both the kinesin and myosin families play multiple roles that in aggregate support the malignant behavior of GBM. For example, while the kinesin family member Kif11 is needed for bipolar spindle formation during mitosis, including in GBM cells, we found that it is also plays an important role in GBM invasion, and its inhibition by highly specific small molecule inhibitors significantly prolongs survival in GBM PDX models *in vivo* (Venere et al., 2015). Likewise, we have shown that targeting myosin II either genetically or pharmacologically blocks both invasion and proliferation in GBM and produces a significant survival advantage in murine models of this disease (Picariello et al., 2019). We have also argued that molecular motors represent points where multiple, redundant proliferation- and invasion-stimulating signaling pathways converge, and as such, their inhibition should produce a robust, sustained anti-tumor effect. Although we have shown this to be the case for both Kif11 and myosin II, pharmacologic inhibition of Kif11 can be myelosuppressive, and genetic knockout of myosin IIA or IIB is lethal in mice (Ma and Adelstein, 2014). By contrast, not only is MYO10 important in both tumor invasion and proliferation but also MYO10 knockout mice can grow to adulthood and breed normally, implying that normal cells can accommodate to loss of this motor. Taken together, our findings highlight important roles that MYO10 plays in driving the malignant phenotype of GBM and they argue that further studies are warranted to validate the potential of a therapeutic strategy that targets this pleiotropic molecular motor.

Limitations of the Study

Much of the work described in this report has relied on well-characterized GEMMs of GBM, and we have used them to demonstrate that genetic deletion of MYO10 has pleiotropic effects in this tumor that have translational potential. Although these GEMMs faithfully recapitulate many of the molecular and histologic features of human GBM, they likely do not reproduce the inter- and intra-tumoral heterogeneities that are typical of the human disease. In this regard, we do note that several of the central conclusions of our report—that MYO10 targeting impairs tumor invasion, slows proliferation, and sensitizes tumor cells to inhibitors of DNA damage repair—are also consistent with our studies of four primary human GBM cell lines. However, validating the importance of MYO10 as a GBM target, identifying the tumor cell subtypes for which its targeting is likely to be effective, and determining how to optimize such a therapeutic approach, will require extensive evaluation of patient-derived xenograft models and will be investigated in future studies in our laboratories.

Resource Availability

Lead Contact

Steven S. Rosenfeld, Mayo Clinic, 4500 San Pablo Road, Jacksonville, FL 32224; rosenfeld.steven@mayo.edu

Materials Availability

All genetically engineered mouse models generated in this study will be made available on request, but we may require a payment and/or a completed Materials Transfer Agreement if there is potential for commercial application. All unique/stable reagents generated in this study are available from the Lead Contact with a completed Materials Transfer Agreement.

Data and Code Availability

Data from the phospho-antibody array is available through Mendeley Data at the following link: Rosenfeld, Steven (2020), "Myosin 10 Phospho Antibody Array," Mendeley Data, V1, https://doi.org/10.17632/5cnvmf9m2d.1.

METHODS

All methods can be found in the accompanying Transparent Methods supplemental file.

SUPPLEMENTAL INFORMATION

Supplemental Information can be found online at https://doi.org/10.1016/j.isci.2020.101802.

ACKNOWLEDGMENTS

This work was supported by NIH grants R01NS073610 and U54CA210910 to S.S.R.; R01NS103473 and R01NS052738 to P.C.; R01CA184803 and U54CA210173 to K.K.; R01CA200399, R01CA195503, and R01CA216855 to A.Q.H.; R01GM134531 to R.C.; R01CA78383 and R01CA150190 to D.M.; T32CA009156 to the Lineberger Cancer Center for E.G.H.; and NSF grant DGE-1746891 to E.W. We wish to thank Dr. Justin D. Lathia (Cleveland Clinic) for the gift of the L1 cell line and Ms. Trine Giaever for illustrations.

AUTHOR CONTRIBUTIONS

Conception and Design: R.S.K, S.S.R., P.C., K.K., R.C., and A.D.

Development of Methodology: R.S.K., S.S.R., K.K., P.M., E.W., E.H., and S.B.

Acquisition of Data: R.S.K., P.M., E.W., E.H., J.F.C., H.S.P., A.L., R.W., N.Z., M.L.-V., T.K., and S.B.

Analysis and Interpretation of Data: R.S.K., A.D., P.M., E.W., R.C., K.K., P.C., and S.S.R.

Administrative, Technical, or Material Support: A.Q.-H., J.A.H., and R.E.C.

DECLARATION OF INTERESTS

The authors declare that they have no competing interests.

Received: September 8, 2020
Revised: October 18, 2020
Accepted: November 10, 2020
Published: December 18, 2020

REFERENCES

Arjonen, A., Kaukonen, R., and Ivaska, J. (2011). Filopodia and adhesion in cancer cell motility. Cell Adh. Migr. *5*, 421–430.

Arjonen, A., Kaukonen, R., Mattila, E., Rouhi, P., Högnäs, G., Sihto, H., Miller, B.W., Morton, J.P., Bucher, E., Taimen, P., et al. (2014). Mutant p53-associated myosin-X upregulation promotes breast cancer invasion and metastasis. J. Clin. Invest. *124*, 1069–1082.

Assanah, M., Lochhead, R., Ogden, A., Bruce, J., Goldman, J., and Canoll, P. (2006). Glial progenitors in adult white matter are driven to form malignant gliomas by platelet-derived growth factor-expressing retroviruses. J. Neurosci. *26*, 6781–6790.

Bae, H.B., Zmijewski, J.W., Deshane, J.S., Tadie, J.M., Chaplin, D.D., Takashima, S., and Abrahamn, E. (2011). AMP activated protein kinase enhances the phagocytic ability of macrophages and neutrophils. FASEB J. *25*, 4358–4368.

Bakhoum, S.F., Kabeche, L., Compton, D.A., Powell, S.N., and Bastians, H. (2017). Mitotic DNA damage response: at the crossroads of structural and numerical cancer chromosome instabilities. Trends Cancer *3*, 225–234.

Bao, S., Wu, Q., McLendon, R.E., Hao, Y., Shi, Q., Hjelmeland, A., Dewhirst, M.W., Bigner, D.D., and Rich, J.N. (2006). Glioma stem cells promote radioresistance by preferential activation of the DNA damage response. Nature *444*, 756–760.

Bidkhori, G., Narimani, Z., Hosseini Ashtiani, S., Moeini, A., Nowzari-Dalini, A., Masoudi-Nejad, A., et al. (2013). Reconstruction of an integrated genome-scale co-expression network reveals key modules involved in lung adenocarcinoma. PLoS One *8*, e67552.

Burger, P.C., and Kleihues, P. (1989). Cytologic composition of the untreated glioblastoma with implications for evaluation of needle biopsies. Cancer *63*, 2014–2023.

Cao, R., Chen, J., Zhang, X., Zhai, Y., Qing, X., Xing, W., Zhang, L., Malik, Y.S., Yu, H., and Zhu, X. (2014). Elevated expression of myosin X in tumours contributes to breast cancer aggressiveness and metastasis. Br. J. Cancer *111*, 539–550.

Cox, D., Berg, J.S., Cammer, M., Chinegwundoh, J.O., Dale, B.M., Cheney, R.E., and Greenberg, S. (2002). Myosin X is a downstream effector of PI(3)K during phagocytosis. Nat. Cell Biol. *4*, 469–477.

Deleyrolle, L.P., Harding, A., Cato, K., Siebzehnrubl, F.A., Rahman, M., Azari, H., Olson, S., Gabrielli, B., Osborne, G., Vescovi, A., and Reynolds, B.A. (2011). Evidence for label-

retaining tumour-initiating cells in human glioblastoma. Brain *134*, 1331–1343.

Dhruv, H.D., McDonough Winslow, W.S., Armstrong, B., Tuncali, S., Eschbacher, J., Kislin, K., Loftus, J.C., Tran, N.L., and Berens, M.E. (2013). Reciprocal activation of transcription factors underlies the dichotomy between proliferation and invasion of glioma cells. PLoS One *15*, e7213410.

Frech, M., Andjelkovic, M., Ingley, E., Reddy, K.K., Falck, J.R., and Hemmings, B.A. (1997). High affinity binding of inositol phosphates and phosphoinositides to the pleckstrin homology domain of RAC/protein kinase B and their influence on kinase activity. J. Biol. Chem. *272*, 8474–8481.

Galli, R., Binda, E., Orfanelli, U., Cipelletti, B., Gritti, A., De Vitis, S., Fiocco, R., Foroni, C., Dimeco, F., and Vescovi, A. (2004). Isolation and characterization of tumorigenic, stem-like neural precursors from human glioblastoma. Cancer Res. *64*, 7011–7021.

Giese, A., and Westphal, M. (1996). Glioma invasion in the central nervous system. Neurosurgery *39*, 235–250.

Hardie, D.G. (2015). AMPK: positive and negative regulation, and its role in whole-body energy homeostasis. Curr. Opin. Cell Biol. *33*, 1–7.

Heimsath, E.G., Jr., Yim, Y.I., Mustapha, M., Hammer, J.A., and Cheney, R.E. (2017). Myosin X knockout is semi-lethal and demonstrates that myosin X functions in neural tube closure, pigmentation, hyaloid vasculature repression, and filopodia formation. Sci. Rep. *6*, 17354.

Kerber, M.L., and Cheney, R.E. (2011). Myosin-X: a MyTH-FERM myosin at the tips of filopodia. J. Cell Sci. *124*, 3733–3741.

Kwon, M., Bagonis, M., Danuser, G., and Pellman, D. (2015). Direct microtubule binding by Myosin 10 orients centrosomes toward retraction fibers and subcortical actin clouds. Dev. Cell *34*, 323–337.

Lathia, J.D., Mack, S.C., Mulkearns-Hubert, E.E., Valentim, C.L.L., and Rich, J.N. (2015). Cancer stem cells in glioblastoma. Genes Dev. *29*, 1203–1217.

Linch, M., Sanz-Garcia, M., Soriano, E., Zhang, Y., Philippe Riou, P., Rosse, C., Cameron, A., Knowles, P., Purkiss, A., Kjaer, S., et al. (2013). A cancer-associated mutation in atypical protein kinase Ci occurs in a substrate-specific recruitment motif. Sci. Signal. *6*, ra82.

Lu, K.V., Chang, J.P., Parachoniak, C.A., Pandika, M.M., Aghi, M.K., Meyronet, D., Isachenko, N., Fouse, S.D., Phillips, J.J., Cheresh, D.A., et al. (2012). VEGF inhibits tumor cell invasion and mesenchymal transition through a MET/VEGFR2 complex. Cancer Cell *22*, 21–35.

Luikart, B.W., Zhang, W., Wayman, G.A., Kwon, C.-H., Westbrook, G.L., Luis, F., and Parada, L.F. (2008). Neurotrophin-dependent dendritic filopodial motility: a convergence on PI3K signaling. J.Neurosci. *28*, 7006–7012.

Luxton, G.W.G., and Gundersen, G.G. (2011). Orientation and function of the nuclear–centrosomal axis during cell migration. Curr. Opin. Cell Biol. *23*, 579–588.

Ma, X., and Adelstein, R.S. (2014). The role of vertebrate nonmuscle myosin II in development and human disease. Bioarchitecture *4*, 88–102.

Makowska, K.A., Hughes, R.E., White, K.J., Wells, C.M., and Peckham, M. (2015). Specific myosins control actin organization, cell Morphology, and migration in prostate cancer cells. Cell Rep. *13*, 2118–2125.

Meley, D., Bauvy, C., houben-Weerts, J.H.P.M., Dubbelhuis, P.F., Helmond, M.T.J., Codogno, P., and Meijer, A.J. (2006). AMP-activated protein kinase and the regulation of autophagic proteolysis. J. Biol. Chem. *281*, 34870–34880.

Miihkinen, M., Grönloh, M.L.B., Vihinen, H., Jokitalo, E., Goult, B.T., Ivaska, J., and Jacquemet, G. (2020). Myosin-X FERM domain modulates integrin activity at filopodia tips. BioRxiv. https://doi.org/10.1101/2020.05.05.078733.

Mistriotis, P., Wisniewski, E.O., Bera, K., Keys, J., Li, Y., Tuntithavornwat, S., Law, R.A., Perez-Gonzalez, N.A., Erdogmus, E., Zhang, Y., et al. (2019). Confinement hinders motility by inducing RhoA mediated nuclear influx, volume expansion, and blebbing. J. Cell Biol. *218*, 4093–4111.

Norden, A.D., Young, G.S., Setayesh, K., Muzikansky, A., Klufas, R., Ross, G.L., Ciampa, A.S., Ebbeling, L.G., Levy, B., Drappatz, J., et al. (2008). Bevacizumab for recurrent glioblastoma. Neurology *70*, 779–787.

Picariello, H.S., Kenchappa, R.S., Rai, V., Crish, J.F., Dovas, A., Pogoda, K., McMahon, M., Bell, E.S., Chandrasekharan, U., Luu, A., et al. (2019). Myosin IIA suppresses glioblastoma development in a mechanically sensitive manner. Proc. Natl. Acad. Sci. U S A *116*, 15550–15559.

Plantard, L., Arjonen, A., Lock, J.G., Nurani, G., Ivaska, J., and Strömblad, S. (2010). PtdIns(3,4,5)P_3 is a regulator of myosin-X localization and filopodia formation. J. Cell Sci. *123*, 3525–3534.

Puduvalli, V.K., and Hoang, N. (2018). Chemotherapy of high grade astrocytomas in adults. Prog. Neurol. Surg. *31*, 116–144.

Raines, A.N., Nagdas, S., Kerber, M.L., and Cheney, R.E. (2012). Headless Myo10 is a negative regulator of full length Myo10 and inhibits axon outgrowth in cortical neurons. J. Biol. Chem. *287*, 24873–24883.

Sandquist, J.C., Larson, M.E., Woolner, W., Ding, Z., and Bement, W.M. (2018). An interaction between myosin-10 and the cell cycle regulator Wee1 links spindle dynamics to mitotic progression in epithelia. J. Cell Biol. *217*, 849–859.

Summerbell, E.R., Mouw, J.K., Bell, J.S.K., Knippler, C.M., Pedro, B., Arnst, J.L., Khatib, T.O., Commander, R., Barwick, B.J., Konen, J., et al. (2020). Epigenetically heterogeneous tumor cells direct collective invasion through filopodia-driven fibronectin micropatterning. Sci. Adv. *6*, eaaz6197.

Sun, Y., Ai, X., Shen, S., and Lu, S. (2015). NF-kappaB-mediated miR-124 suppresses metastasis of non- small-cell lung cancer by targeting MYO10. Oncotarget *6*, 8244–8254.

Thorne, R.G., and Nicholson, C. (2006). In vivo diffusion analysis with quantum dots and dextrans predicts the width of brain extracellular space. Proc. Natl. Acad. Sci. U S A *103*, 5567–5572.

Tokuo, H., Bhawan, J., and Coluccio, L.M. (2018). Myosin X is required for efficient melanoblast migration and melanoma initiation and metastasis. Sci. Rep. *8*, 10449.

Towler, M.C., and Hardie, D.G. (2007). AMP-activated protein kinase in metabolic control and insulin signaling. Circ. Res. *100*, 328–341.

Venere, M., Hamerlik, P., Wu, Q., Rasmussen, R.D., Song, L.A., Vasanji, A., Tenley, N., Flavahan, W.A., Hjelmeland, A.B., Bartek, J., and Rich, J.N. (2014). Therapeutic targeting of constitutive PARP activation compromises stem cell phenotype and survival of glioblastoma-initiating cells. Cell Death Diff. *21*, 258–269.

Venere, M., Horbinski, C., Crish, J.F., Jin, X., Vasanji, A., Major, J., Burrows, A.C., Chang, C., Prokop, J., Wu, Q., et al. (2015). The mitotic kinesin Kif11 is a driver of invasion, proliferation, and self-renewal in glioblastoma. Sci. Transl. Med. *7*, 304ra143.

Woolner, S., O'Brien, L.L., Wiese, C., and Bement, W.M. (2008). Myosin 10 and actin filamentrs are essential for mitotic spindle function. J. Cell Biol. *182*, 77–88.

Yang, J.M., Schiapparelli, P., Nguyen, H.N., Igarashi, A., Zhang, Q., Abbadi, S., Amzel, L.M., Sesaki, H., Quinones Hinojosa, A., and Iijima, M. (2017). Characterization of PTEN mutations in brain cancer reveals that pten mono-ubiquitination promotes protein stability and nuclear localization. Oncogene *36*, 3673–3685.

Zhang, H., Berg, J.S., Li, Z., Wang, Y., Lang, P., Sousa, A.D., Bhaskar, A., Cheney, R.E., and Stromblad, S. (2004). Myosin-X provides a motor-based link between integrins and the cytoskeleton. Nat. Cell Biol. *6*, 523–531.

Zhao, R., Afthinos, A., Zhu, T., Mistriotis, P., Li, Y., Serra, S.A., Zhang, Y., Yankaskas, C.L., He, S., Valverde, M.A., et al. (2019). Cell sensing and decision making in confinement: the role of TRPM7 in a tug of war between hydraulic pressure and cross sectional area. Sci. Adv. *5*, eaaw7243.

iScience, Volume *23*

Supplemental Information

Myosin 10 Regulates Invasion, Mitosis, and Metabolic Signaling in Glioblastoma

Rajappa S. Kenchappa, Panagiotis Mistriotis, Emily Wisniewski, Santanu Bhattacharya, Tanmay Kulkarni, Rita West, Amanda Luu, Meghan Conlon, Ernest Heimsath, James F. Crish, Hannah S. Picariello, Athanassios Dovas, Natanael Zarco, Montserrat Lara-Velazquez, Alfredo Quiñones-Hinojosa, John A. Hammer, Debrabrata Mukhopadhyay, Richard E. Cheney, Konstantinos Konstantopoulos, Peter Canoll, and Steven S. Rosenfeld

Figure S1: MYO10 deletion reduces growth of murine GBM. Related to Figure 1

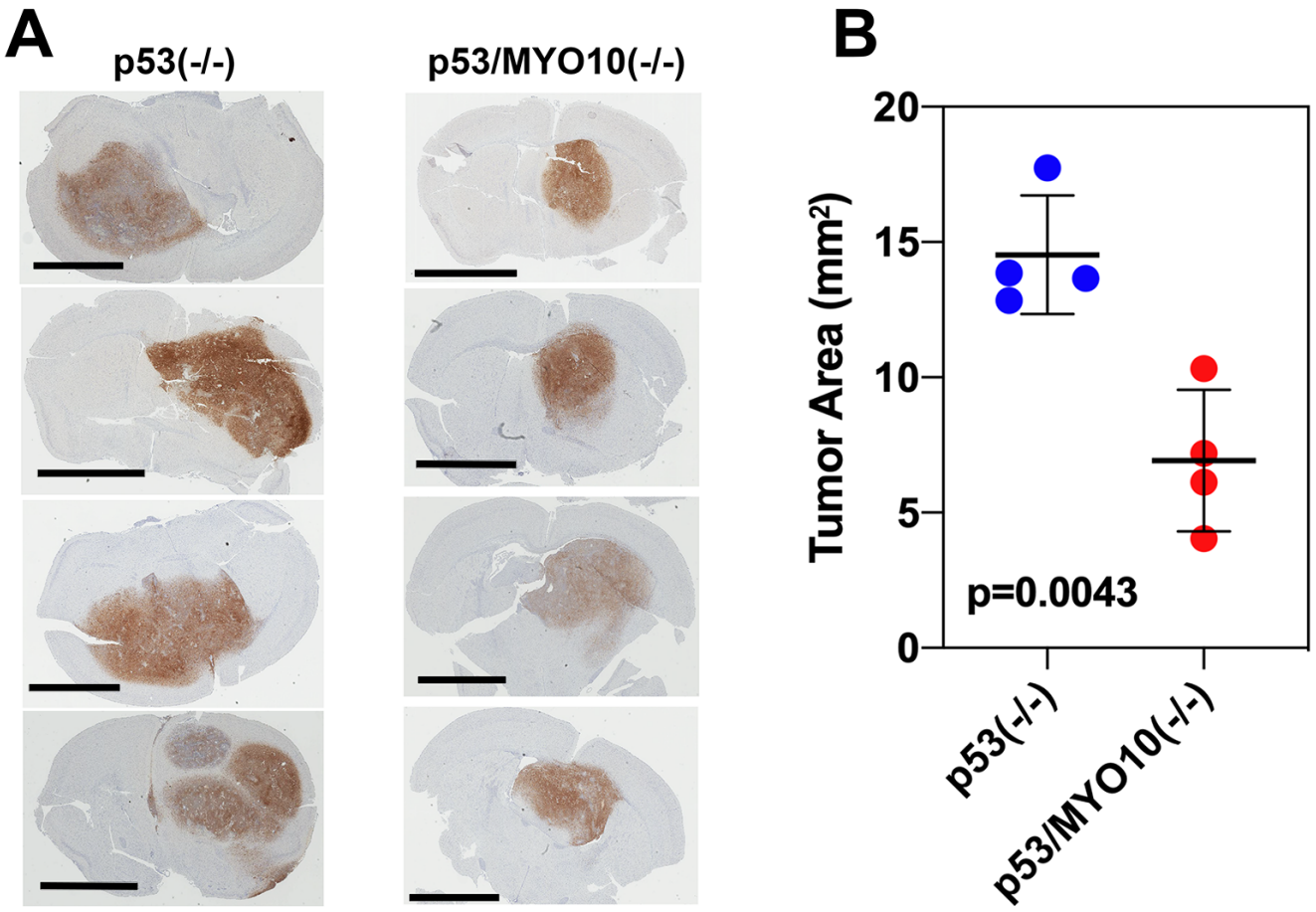

Figure S2: Fluorescence staining of PTEN(-/-) cells for F-actin and MYO10 distribution. Related to Figure 2

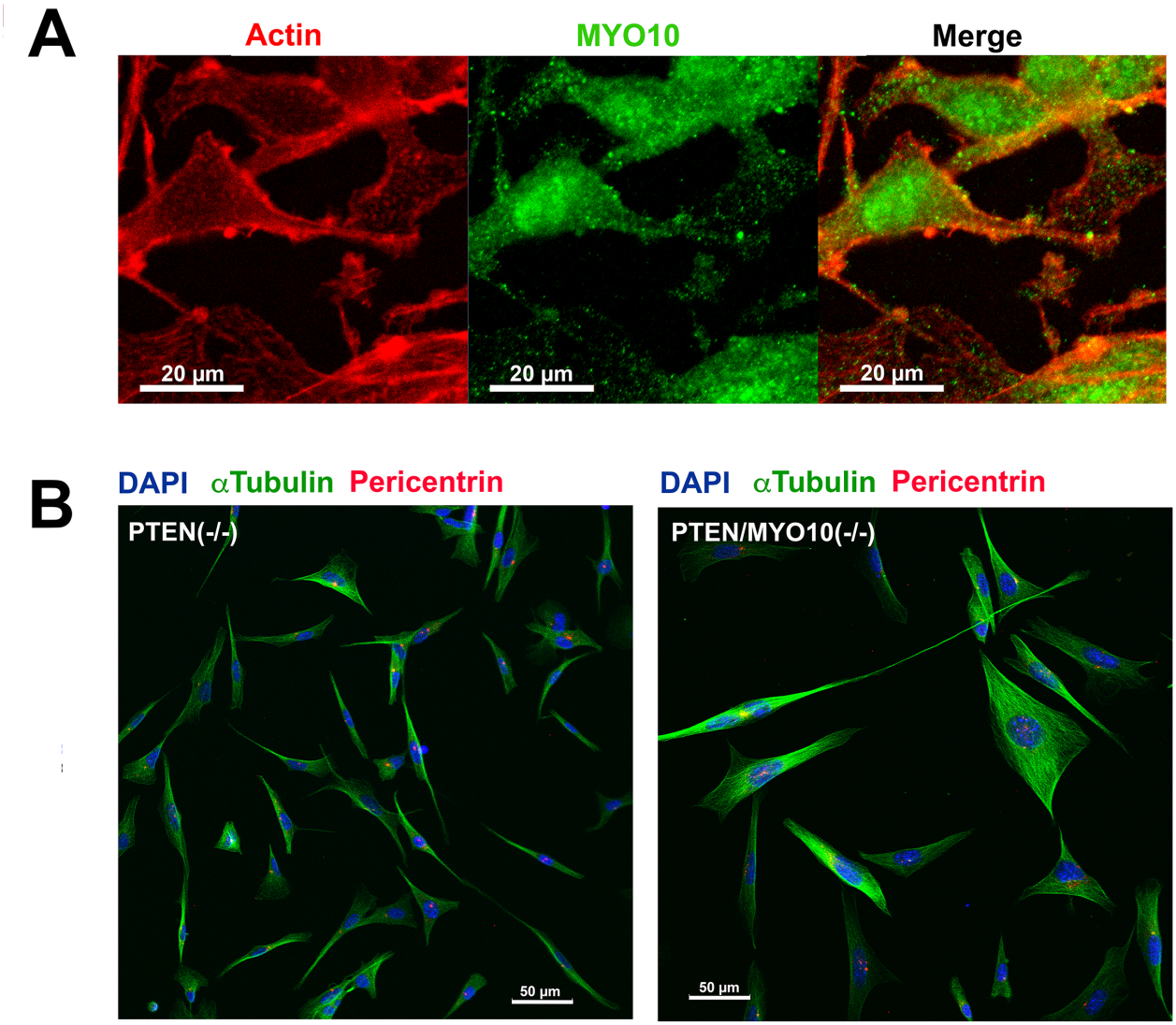

Figure S3: MYO10 suppression with shRNA impairs invasion and slows proliferation in three primary human GBM cell lines. Related to Figure 4

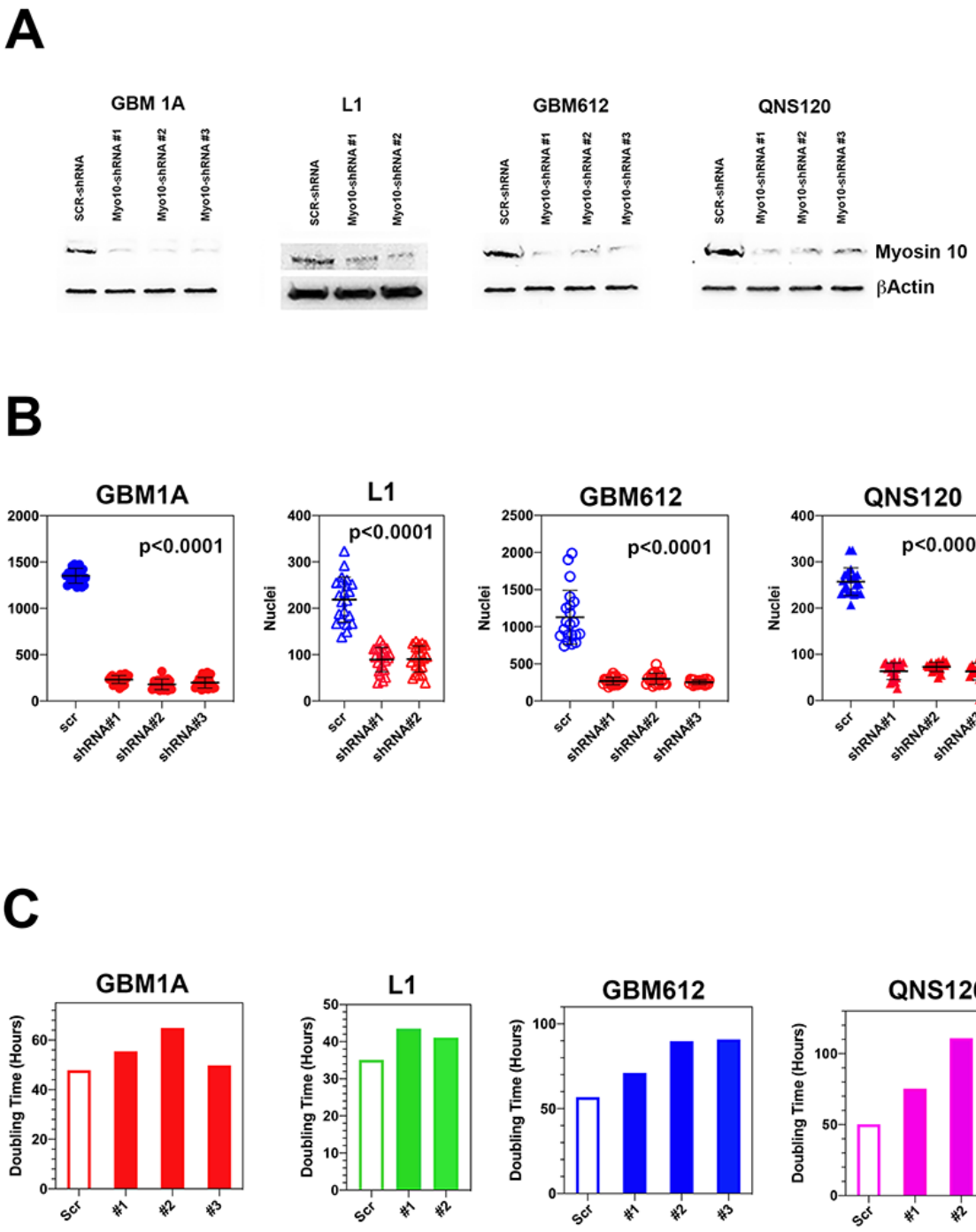

Figure S4: MYO10 deletion enhances the DNA damage response. Related to Figure 5.

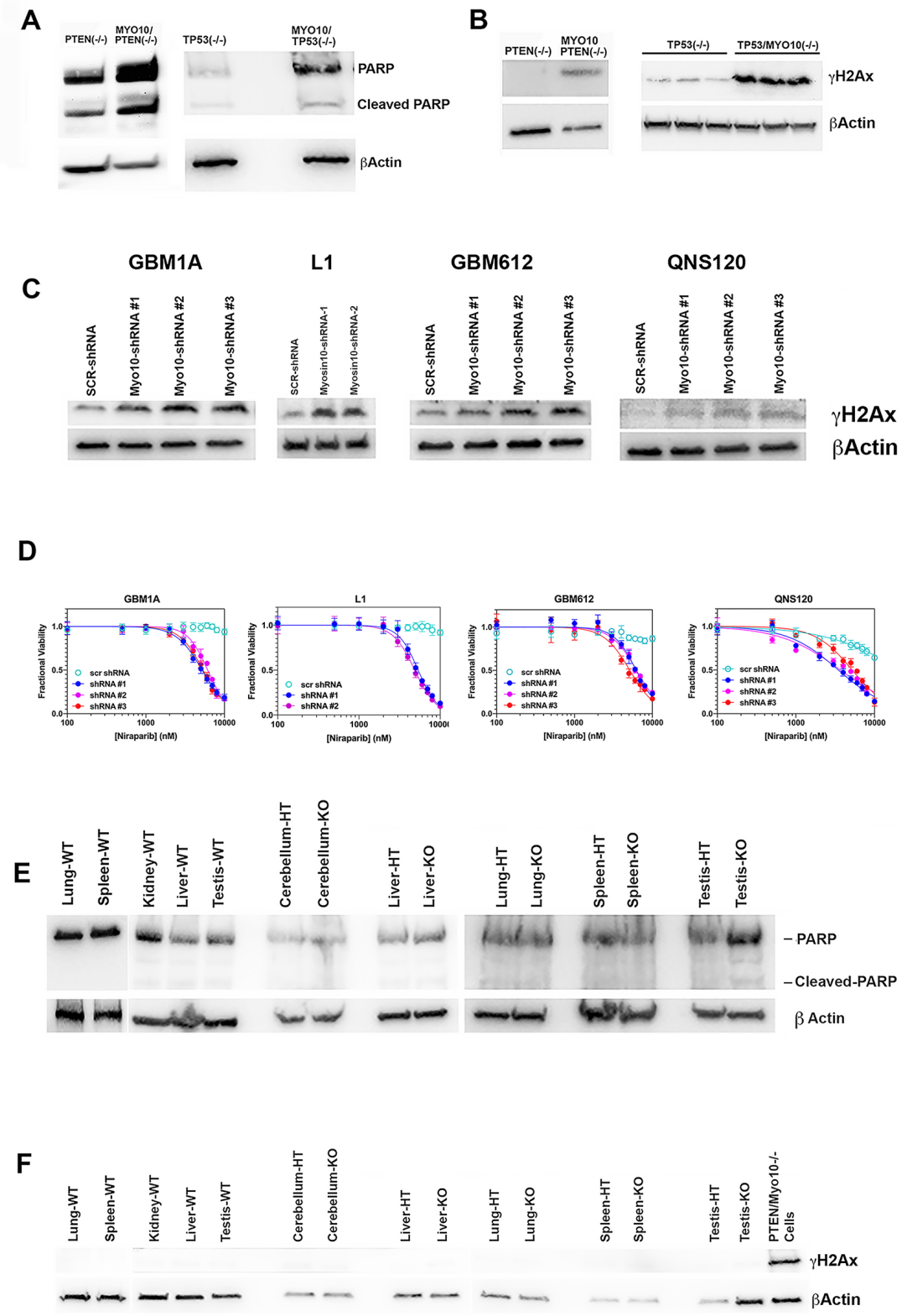

Figure S5: MYO10 deletion alters AMPK and AKT signaling in a PTEN-dependent manner. Related to Figure 6.

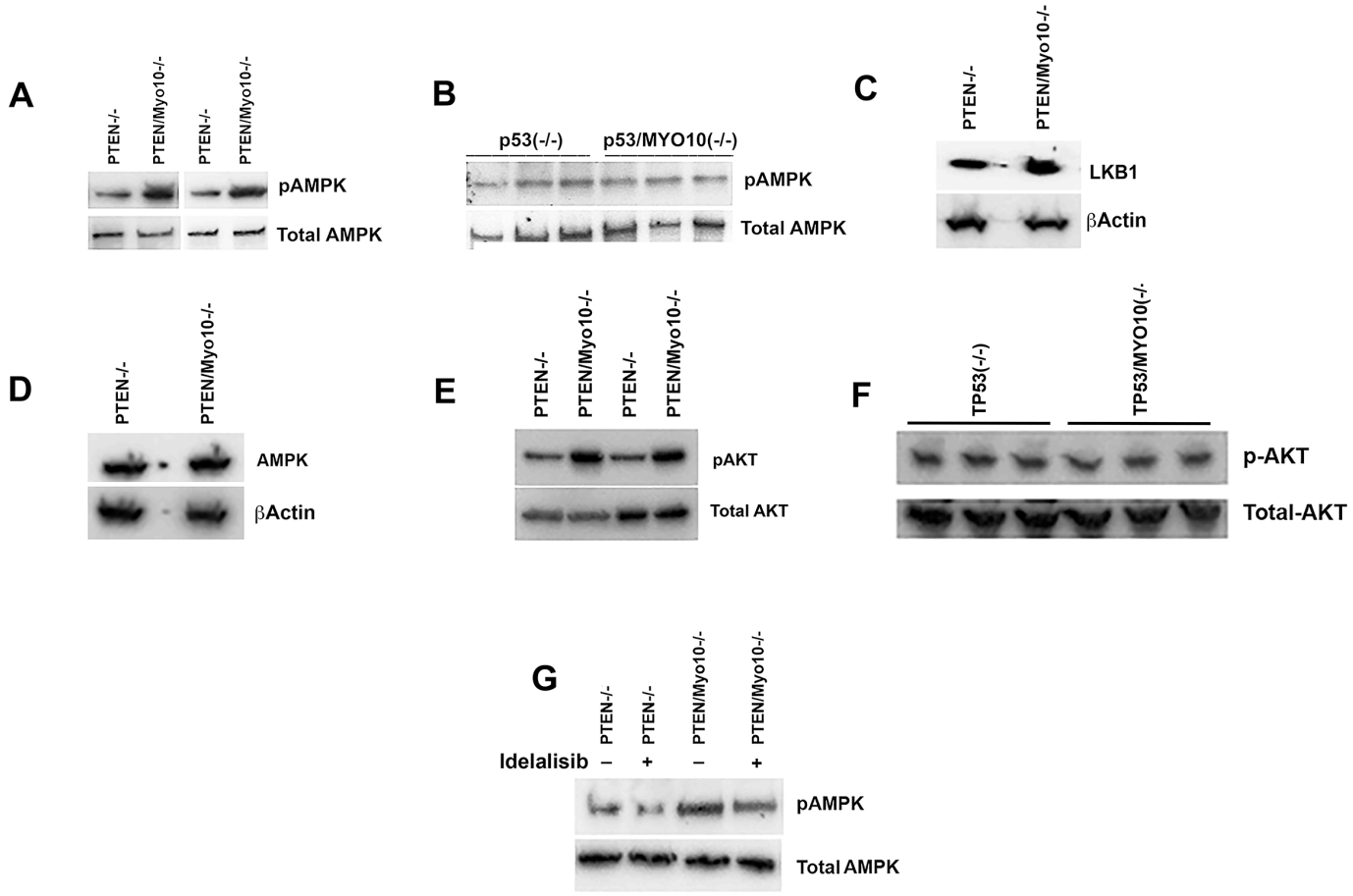

Figure S6: Suppression of MYO10 expression in PTEN(-/-) cells with shRNA recapitulates the effects on DNA damage and AMPK phosphorylation seen with genetic deletion of this motor. Related to Figure 6.

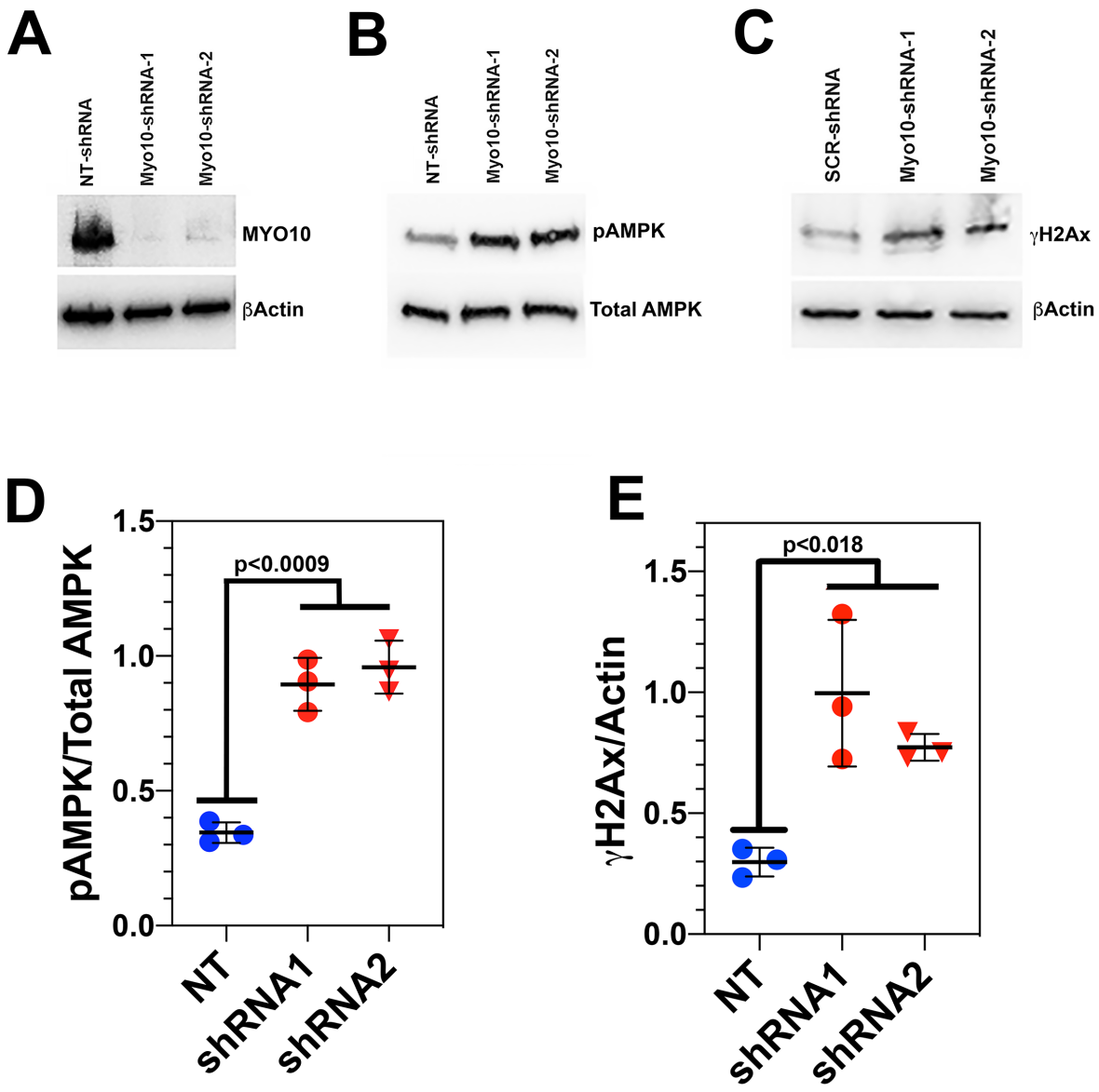

Figure S7: Effect of expression of a GFP-PH domain from AKT (A-D) or of full length GFP-MYO10 (E-H) on AMPK phosphorylation and γH2Ax expression. Related to Figure 6.

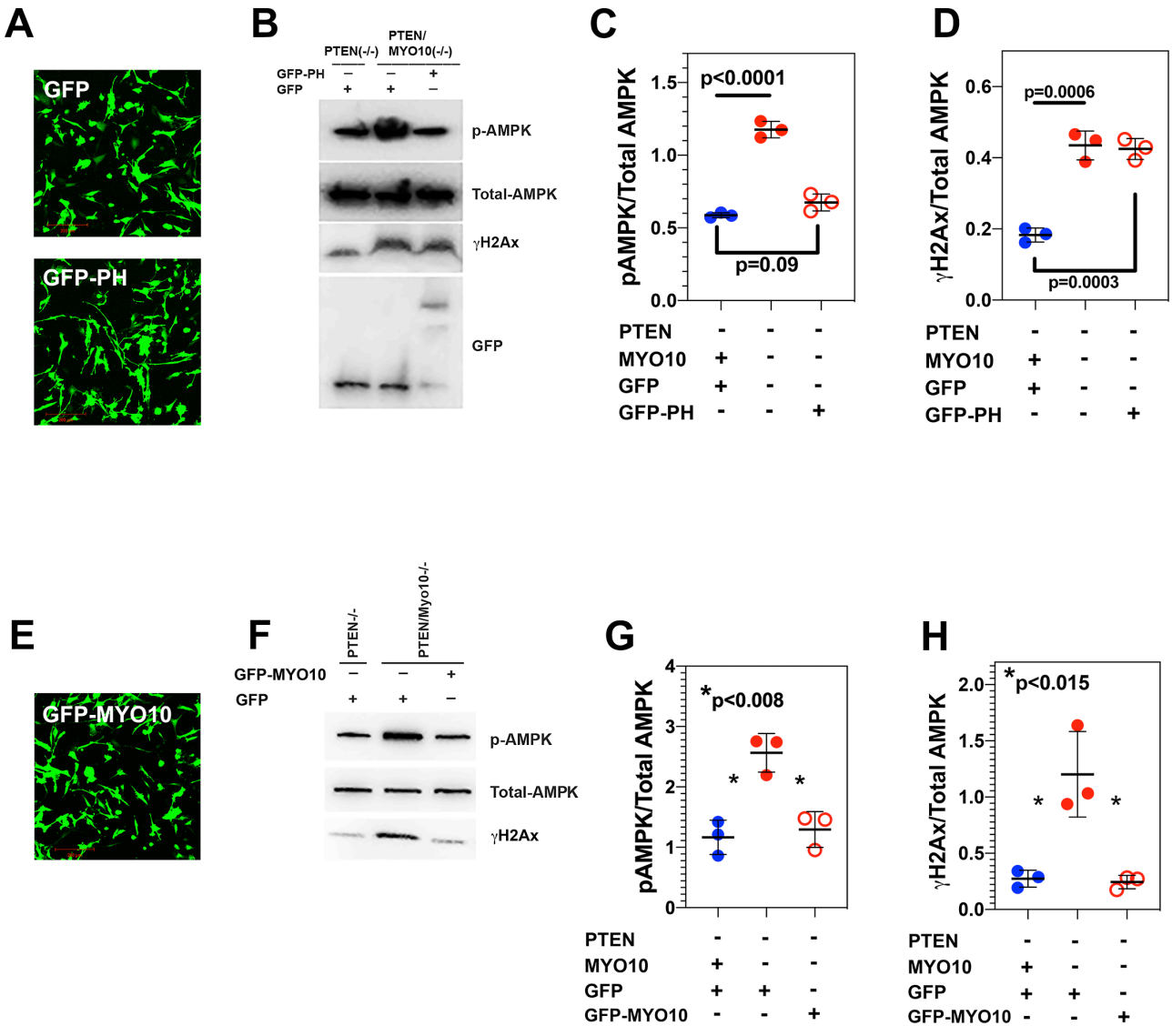

SUPPLEMENTAL FIGURE LEGEND

Figure S1: MYO10 deletion reduces growth of murine GBM. (A). Histologic sections through the center of tumors from four mice with p53(-/-) (*left*) and four mice with p53/MYO10(-/-) (*right*) tumors stained for the HA epitope. Scale bars denote 3 mm **(B).** Area of anti-HA staining in these histologic sections from mice with p53 (-/-) (*blue*) and p53/MYO10 (*red*) tumors. Error bars denote mean ± 1SD. Differences between areas of the two groups are statistically significant (*two tailed t test*).

Figure S2: Fluorescence staining of PTEN(-/-) cells for F-actin and MYO10 distribution. (A). (*Left*) Rhodamine phalloidin staining of permeabilized PTEN(-/-) cells reveals actin staining is largely limited to the cell cortex. (*Middle*) MYO10 demonstrates punctate staining diffusely across the cytoplasm, including in areas of membrane ruffles (*Left*), which includes filopodia. Scale bar denotes 20 μm. **(B).** A field of PTEN(-/-) (*left*) and PTEN/MYO10(-/-) (*right*) cells stained for a tubulin (*green*), pericentrin (*red*), and DAPI (*magenta*) demonstrates that among cells deleted for MYO10, a majority demonstrate multiple spots of pericentrin immunoreactivity, suggesting centrosome fragmentation and/or duplication. Scale bar denotes 50 μm.

Figure S3: MYO10 suppression with shRNA impairs invasion and slows proliferation in three primary human GBM cell lines. (A). Western blots demonstrating MYO10 knockdown in GBM1A, L1, GBM612, and QNS120**. (B).** *In vitro* invasion through a 3μm pore Transwell for these four cell lines transfected with one scrambled (*scr*) and MYO10-suppressing shRNAs. Suppression of MYO10 significantly reduces Transwell invasion in all four lines (*p<0.0001 by one way ANOVA*). Error bars denote mean ± 1SD. **(C).** MYO10 suppression moderately prolongs doubling time in the four cell lines.

Figure S4: MYO10 deletion enhances the DNA damage response. (A). Western blots of PARP and cleaved PARP for PTEN(-/-) and PTEN/MYO10(-/-) cells (*left*) and for TP53(-/-) and TP53/MYO10(-/-) cells (*right*) show that MYO10 deletion enhances both PARP and cleaved PARP levels in both PTEN and TP53-deleted backgrounds. **(B).** Western blots of γH2Ax also show an increase in expression with MYO10 deletion in both PTEN and TP53-deleted backgrounds. **(C).** Expression of γH2Ax is also increased in human glioblastoma cell lines GBM1A, L1, GBM612, and QNS120 with suppression of MYO10. **(D).** Niraparib dose response curves for human glioblastoma cell lines GBM1A, L1, GBM612, and QNS120 treated with scrambled or MYO10 targeting shRNA. Suppression of MYO10 increases sensitivity to niraparib >25 fold in each case. **(E).** PARP expression from tissue derived from wild type C57Bl6 mice (WT), MYO10 heterozygous knockout mice (HT), and MYO10 homozygous knockout mice (KO). **(F).** γH2Ax expression from tissue derived from wild type C57Bl6 mice (WT), MYO10 heterozygous knockout mice (HT), and MYO10 homozygous knockout mice (KO).

Figure S5: MYO10 deletion alters AMPK and AKT signaling in a PTEN-dependent manner. (A). Representative Western blots for phospho-AMPK and total AMPK in MYO10 intact and deleted murine GBM lines deleted for PTEN show enhanced AMPK phosphorylation with MYO10 deletion **(B).** MYO10 deletion in GBM lines deleted for TP53 does not appreciably alter AMPK phosphorylation. **(C).** Western blot of LKB1 in PTEN(-/-) and PTEN/MYO10(-/-) cells show increased LKB1 expression with MYO10 deletion. **(D).** Western blot of total AMPK in PTEN(-/-) and PTEN/MYO10(-/-) cells shows no appreciable change in total AMPK with MYO10 deletion. **(E).** Western blot of phosphoAKT and total AKT in PTEN(-/-) and PTEN/MYO10(-/-) cells. **(F).** Western blot of phospho AKT and total AKT in TP53(-/-) and TP53/MYO10(-/-) cells shows no appreciable effect of MYO10 deletion. **(G).** Effect of the PI3K inhibitor idelalisib on AMPK phosphorylation in PTEN(-/-) and PTEN/MYO10(-/-) cells.

Figure S6: Suppression of MYO10 expression in PTEN(-/-) cells with shRNA recapitulates the effects on DNA damage and AMPK phosphorylation seen with genetic deletion of this motor. (A-C). PTEN(-/-) cells were stably transfected with shRNA-encoding lentiviral particles that were non-targeting (*NT*) or targeted using two distinct MYO10-suppressing vectors. Expression of MYO10 (A), pAMPK and total AMPK (B), and gH2Ax (C) were detected by Western blot. **(D,E).** Quantitation of the Western blot data for pAMPK/total AMPK **(D)** and γH2Ax/βActin **(E)** demonstrates that suppression of MYO10 in PTEN(-/-) cells

has the same effect as its deletion. Error bars denote mean ± 1SD. P values determined from a two tailed t test.

Figure S7: Effect of expression of a GFP-PH domain from AKT (A-D) or of full length GFP-MYO10 (E-H) on AMPK phosphorylation and γH2Ax expression. (A). Live cell imaging of GFP (upper panel) and GFP-PH (lower panel) expression in PTEN/MYO(-/-) cells after two days of transient transfection with the corresponding plasmids. **(B).** Cell lysates were generated 2 days after transfection and probed on Western blot for phospho AMPK, total AMPK, γH2Ax, and GFP. Expression of a GFP-PH fusion protein reduces AMPK phosphorylation levels to those resembling control, GFP-expressing PTEN(-/-) cells, while it does not alter the increase in γH2Ax expression seen with MYO10 deletion. The lower blot also demonstrates that cells transfected with a GFP-expressing plasmid express GFP at the expected molecular weight (M_r *26,886 kDa*) while for cells transfected with the PH-GFP plasmid, the GFP immunoreactive band migrates at the molecular weight expected for a GFP-PH fusion protein (M_r *47,609 kDa*). **(C).** Quantitation of the Western blot data in **(A)** shows that transfecting PTEN/MYO10(-/-) cells with a GFP-PH encoding plasmid reduces normalized pAMPK levels to those resembling control PTEN(-/-) cells. **(D).** Transfection of PTEN/MYO10(-/-) cells with a GFP-PH encoding plasmid does not appreciably alter levels of γH2Ax in these cells. **(E).** Live cell imaging GFP-MYO10 expression in PTEN/MYO(-/-) cells after two days of transient transfection with the corresponding plasmid. **(F-H).** PTEN(-/-) cells were transiently transfected with a GFP-encoding plasmid, and GFP/MYO10(-/-) cells were transiently transfected with either a GFP or GFP-full length MYO10 encoding plasmid. Cell lysates were generated 2 days after transfection and probed on Western blot for phospho AMPK, total AMPK, and γH2Ax. Expression of a GFP-MYO10 fusion protein reduces both AMPK phosphorylation **(G)** and γH2Ax **(H)** levels to those resembling control, GFP-expressing PTEN(-/-) cells. Error bars denote mean ± 1SD. P values determined from two tailed t test.

TRANSPARENT METHODS

Human tissue samples

Patient primary tissue specimens for Western blotting were obtained at the Mayo Clinic, Florida under the approval of the Institutional Review Board (IRB 16008485) and established from excess tissue from patients undergoing surgical resection for glioblastoma or intractable epilepsy.

Mice

All mouse procedures were performed in compliance with protocols approved by the Institute Animal Care and Use Committees at the Mayo Clinic. The homozygous floxed PTEN mice (Stock #006440, Strain Name: $Pten^{tm1Hwu}$) and floxed p53 mice (Stock #008462, Strain Name: $Trp53^{tm1Brn}$) were obtained from Jackson Laboratory. These mice were bred with homozygous floxed Myosin10 (Strain Name: $Myo10^{tm1c/tm1c}$) mice generously provided by Dr. Richard Cheney at the University of North Carolina at Chapel Hill. NOD-SCID mice also obtained from Jackson laboratory (Stock #005557). Experiments were conducted on mice between 10-30 weeks of age. Survival and bioluminescence studies were performed on equal numbers of male and female mice.

Retrovirus production and intracerebral injections

The PDGF-IRES-cre retrovirus was generated according to methods described previously (Lei et al., 2011). Self-inactivating bicistronic expression vectors consisting of a 0.8 kb fragment encoding for a PDGF-B hemagglutinin (HA) fusion protein were cloned into the first multiple cloning site of the pQC-X-I-X vector (Clontech). Replication-deficient retroviruses pseudo-typed with VSV-G coats were produced by transient transfection of GP2-293 cells. Viral supernatants were collected at 36 hr post-transfection. Subsequently, the viral supernatant was concentrated by high-speed centrifugation, and the concentrated virus stock was resuspended in Opti-MEM media. The viral titer was determined by transducing RiboTag cells with serial 1:10 dilutions from the concentrated virus stock in a total volume of 1 ml. At 48 hr after infection, HA positive cell clusters were determined by immunofluorescence with a secondary antibody to HA.

For intracranial retrovirus injection, mice floxed for PTEN, for TP53, for PTEN and MYO10, and for TP53 and MYO10 (8-10 weeks post-natal) were anesthetized with isoflurane. The mice were immobilized on a stereotactic fixation instrument (Kopf Model 926, Brain Tree). A lateral incision of the scalp was made and the skull exposed. A burr hole was made through the skull (Micro-Drill, Cellpoint Scientific Inc) whose location was determined by the stereotactic coordinates relative to the bregma: 2 mm rostral and 2 mm lateral. One microliter of retrovirus at a titer of 10^6 CFU/ml was injected at a depth of 1.5 mm through the burr hole at a rate of 0.2 µl/min with a Hamilton syringe (Model 801, Hamilton Company). To avoid retrovirus extrusion, the Hamilton needle (Hamilton, Cat No. 7762-01) was left in place for two minutes before withdrawal at a speed of 1 mm per minute. The mice were observed daily and sacrificed when they showed symptoms of morbidity and generated Kaplan-Meier survival curves.

In some experiments, mice floxed for TP53 or for TP53 and MYO10 were injected with PDGF-IRES-cre retrovirus as described above. 5 days post retroviral injection, animals from each category were divided into two groups and were treated with 5 days/week dosing of vehicle or 25mg/kg body weight of PARP inhibitor niraparib (Selleck, cat #S7625*)* by intraperitoneal injection. Treatment continued until signs of tumor morbidity developed, at which point mice were sacrificed.

Glioma cell line isolation from mouse GBM tumor and culture:

The protocol for primary tumor isolation has been described (Lei *et al.,* 2011). Selection of the euthanasia method was based on the IACUC guidelines of the Mayo Clinic. Each cell line was isolated from one GBM tumor-bearing mouse that was deeply anesthetized, as demonstrated by loss of nose, tail and hind limb pinch response, with an intraperitoneal injection of a mixture of ketamine (150 mg/kg) and xylazine (15 mg/kg). After decapitation, an *ex-vivo* gross total resection of the tumor was performed and the tumor region was minced with a razor blade. Tumor tissue was resuspended in 2.5% TrypLE (Gibco 12604-013) 1X Anti Anti 100X (Gibco 15240-062) for enzymatic and mechanical dissociation. First, cells were incubated for 5 minute in a 37 °C shaking bath, followed mechanical dissociation using two different sized needles (i.e. 16 ½ G and 18 ½ G). After the dissociation, cells were filtered through a 40µm mesh (BD Falcon) into DMEM media containing 10% heat-inactivated FBS in order to inactivate the trypsin. Cells were centrifuged for 3 minutes at 1000 RPM, and then re-suspended and grown in murine GBM media supplemented with 10 ng/ml PDGF-AA (Sigma P3076), 10 ng/ml FGFb (Sigma F0291), N2 supplement (Gibco), 0.5% FBS, and

penicillin/streptomycin/amphotericin (Invitrogen) in DMEM (Gibco). Primary glioma cells were grown on tissue culture plates coated with 10µg/mL Fibronectin (Sigma F1141).

Transfection of GBM cells

PTEN deleted and PTEN/MYO10 co-deleted murine GBM cells were plated to 70% confluency in 6 well plates and chamber slides. At 24 hours after plating, cells were transfected using jetPRIME transfection reagent according to the manufacturer's instructions. Briefly, pcDNA3-EGF (Addgene plasmid #13031), PH-Btk-GFP (Addgene plasmid # 51463), and EGFPC1-hMyoX (Addgene plasmid #47608) were mixed with jetPRIME buffer. Then jetPRIME reagent was incubated at room temperature for 10 minutes and transfection mixture was added to the cell culture, which was incubated for 48 hours before using for biochemical assays. Transfection efficiency was evaluated by the quantitation of GFP positive cells with confocal microscopy (Zeiss). Human GBM cell lines were transfected with the following shRNAs to suppress MYO10, all from Sigma Aldrich: Myosin10-shRNA-1 (TRCN0000298630), Myosin10-shRNA-2 (TRCN0000286557), Myosin10-shRNA-3 (TRCN0000286489)

Lentiviral production and transduction

Knockdown of MYO10 in murine GBM cells was achieved via lentiviral infection with shRNA-encoding constructs. The lentiviral plasmid vector pLKO.1-puro based shRNA clones and control shRNA vector were purchased from Sigma-Aldrich (St Louis, MO, USA). The following constructs were used for murine GBM cells in these studies: Non Targeting control (SHC002); MYO10 sh-RNA [TRCN0000306003 (MYO10-shRNA-1), TRCN0000375033 (MYO10-shRNA-2). Each of the pLK0.1 targeting constructs were co-transfected with psPAX2 and pMD plasmids into HEK-293T cells via Lipofectamine 3000 transfection agent (Life Technologies, catalog # 11668027) in serum-free medium. After 8 hours of transfection, the viral particle-containing medium was removed and replaced with fresh complete medium. Transfected cells were then grown in DMEM media containing 10% FBS for 48 hours at 37ºC, 5% CO_2. Media containing virus was harvested and centrifuged for 10 mins in a clinical specimen centrifuge and then filtered through a 0.45 µm filter. Lentiviral particles were concentrated using LentiX-Concentrator reagent (Takara Bio USA) and the viral titer was determined using a p24 ELISA kit (Clontech). Mouse glioma cells were infected by incubating with virus containing media (10 MOI of virus and 4µg/mL of polybrene (Sigma-Aldrich)) overnight. Cells were selected for positive shRNA infection using puromycin (0.5ug/ml) for seven days and maintained in 0.1ug/mL puromycin containing media.

Proliferation assays

Murine GBM cells were plated at 1000 cells/well in 96-well plates. The plate was scanned and phase-contrast images (4 per well) were acquired in real time every 12 hours for 6 days using the Cytation 5 Cell Imaging Multi-Mode Reader (BioTek Instruments, Inc). We also utilized Softwell 96 HTS plates (Matrigen) to determine the effect of loss of MYO10 on proliferation over a range of substrate stiffness. These 96 well plates contain one column each of 0.2, 0.5, 1, 2, 4, 8, 12, 25, and 50 kPa hydrogels that are coated with fibronectin. The plate was scanned as above for every 12 hours for 6 days using Cytation 5. Cell counts per well at each time point were quantified and cell count versus time was fit to a set of exponential growth equations to calculate growth rate constants for each condition (Prizm).

Cell viability assays

To determine the effect of inhibitors of PARP, AMPK and PI3 Kinase on cell viability, murine GBM cells were plated at 5000 cells/well in 96-well plates. After 48 hrs, cells were treated with a range of concentrations of inhibitors of PARP (Niraparib; Selleck, cat #S7625), AMPK (Dorsomorphin; Selleck, cat #S7305), PI3K (Idelalisib; Selleck, cat #S2226) or vehicle (DMSO). After an additional 72 hrs, cell viability was determined using an ATP-dependent cell viability assay (Cell Titer Glo) and data was normalized to cells treated with vehicle.

Immunofluorescece measurements

Cells were grown on fibronectin (10 µg/ml) coated glass chamber slides and fixed with ice-cold 4% paraformaldehyde for 15 minutes at room temperature. After washing with PBS three times, cells were permeabilized with 0.1% Triton X-100 PBS, and then washed three more times with PBS. Cells were incubated with 10% goat serum in PBST (PBS+ 0.1% Tween 20) for 1hr to block non-specific binding of the antibodies. The primary antibodies (Anti Myosin 10, Novus Biologicals, cat #22430002, diluted 1:800; Anti

γ-tubulin, Santa Cruz Biotech sc-17787, diluted 1:100; Anti Pericentrin, Abcam, cat #ab220784, diluted 1:2000) in 2% goat serum in PBST was incubated with cells overnight at 4°C. Following washing, a secondary antibody (goat anti-rabbit IgG-Alexa 488 (for Myosin 10 staining), Molecular Probes, cat #A32731) (goat anti-mouse IgG-Alexa 594 (for γ-tubulin staining), Molecular Probes, cat #A11005) and goat anti-rabbit IgG-Alexa 488 (for Pericentrin staining), Molecular Probes, Molecular Probes, cat #A32731) diluted 1:500 in PBST was applied to cells and incubated 1 hr at room temperature in the dark. Cells were stained for F-actin with Rhodamine Phalloidin (Cytoskeleton Inc, cat #PHDR1, diluted to 100nM final concentration) for 30 minutes. The slides were then mounted with cover slips using Vectashield (#H-1200; Vector Laboratories). Cells were visualized and imaged using confocal microscopy (Zeiss).

Brain histological and immunohistochemical analysis

Each GBM tumor bearing mouse was deeply anesthetized with intraperitoneal injection of a mixture of ketamine (150 mg/kg) and xylazine (15 mg/kg) as demonstrated by loss of nose, tail and hind limb pinch response—a euthanasia method based on the IACUC guidelines of the Mayo Clinic. As described previously (36), mice were perfused by intracardiac injection with 15 ml ice cold PBS, followed by 15 ml cold 4% paraformaldehyde (PFA). Brains were removed and fixed overnight at 4 degrees in 4% PFA. Brains were paraffin embedded and microtome sectioned (5 μm thick) and then processed for histological analysis. Immunohistochemical staining was performed using the Discovery ULTRA automated stainer from Ventana Medical System Inc. (Tuscon, AZ). In brief, antigen retrieval was performed using a Tris/borate/EDTA buffer (Discovery CC1, 06414575001; Ventana), pH 8.0 to 8.5, for 64 minutes at 95°C. Slides were incubated with anti Ki67 at 1:1000 (VP-K451, Vector Laboratories) or HA at 1:1000 (11 867 423 001, Sigma-Aldrich), for 2 Hours at Room Temperature. The antibodies were visualized using biotinylated goat anti-rabbit and rabbit anti-rat secondary at 1:200 (BA-1000/BA-4001; Vector Laboratories, Burlingame, CA) and the DABMap detection kit (0526636001; Ventana). Finally, the slides were counterstained with hematoxylin and bluing and images were captured and analyzed using a ScanScope scanner and ImageScope software (Aperio Technologies).

Transwell migration assays

Flouroblok Transwell inserts were coated with 5 μg/ml laminin (Sigma L2020-1MG) for 1 hr at 37ºC, then washed with PBS before adding 125000 cells for each insert. The Transwells were inserted into wells containing 10% FBS in glioma media as a chemoattractant. Cells were incubated for 15 hours at 37ºC, the Transwells were then washed with PBS, fixed in 4% PFA for 15 min and then washed twice more with PBS before staining with DAPI. Images were captured and analyzed for nuclear count using Cytation 5 (BioTek Instruments, Inc).

Cell migration experiments

Confined cell migration experiments were performed as previously described (Zhao *et al.,* 2019; Mistriotis *et al.,* 2019). Briefly, polydimethylsiloxane (PDMS)-based microfluidic devices were fabricated by multilayer photolithography (Paul *et al.,* 2019), with either a straight channel configuration (200 μm *L,*10, 6, and 3 μm *W* x 10 μm *H*) or a trifurcating configuration (Feeder Channel: 200 μm *L*, 10 μm *W*, *H*; Left Branch, Center Branch: 10 μm *W*,*H*; Right Branch: 20 μm *W*, 10 μm *H*) . Channels were coated with fibronectin (Sigma F1141, 10 μg/mL) at 37˚C for 1 hour prior to cell seeding. For device seeding, cells were resuspended at a concentration of 5 $X10^6$ cells/mL, then 20-40 μL of cell suspension was added to each device. After cells had adhered, all wells of the device were filled with 100 μL BFP Media. Cells were imaged every 10 to 20 min for 24 hours on an inverted Nikon Eclipse Ti microscope (Nikon) with automated controls (NIS-Elements; Nikon) and a 10X/0.45 NA Ph1 objective using time-lapse microscope. Cells were maintained at 37˚C, 5% CO_2 using a controlled stage top incubator (Okolab or Tokai). Time-lapse videos were exported to ImageJ (National Institutes of Health). Cell migration was tracked using the MTrackJ plugin. A custom MATLAB (MathWorks) script was used to calculate cell speed and persistence from migration tracks. Cell decision making analysis was performed manually. Decision time was identified as the time when the cell body first reached the trifurcation until the time when 90% of the cell body had entered one of the trifurcating channels.

Cell cycle analysis

Cell cycle analysis was performed using Click-iT EdU Flow cytometry Cell Proliferation Assay kit (Invitrogen catalog# C10424) according to the manufacturer's instructions. Briefly, cells were seeded on 6-cm dishes and incubated during 2 hours with 10μM EdU. Then cells were harvested, permeabilized and

fixed, followed by resuspension in 500 µL of saponin-based permeabilization and wash reagent. Fixed cells were incubated in RNase A for 1 hour, followed by an incubation in DAPI for 5 min at 4 °C. Cellular DNA content was analyzed on an Attune NxT flow cytometer, and data were analyzed with Attune NxT software.

Live cell imaging

PTEN deleted and PTEN/MYO10 co-deleted murine GBM cells were seeded onto 35 mm glass bottom dishes (MatTek #P35G-20-1.5C) coated with 10 ng/mL fibronectin (Sigma #F1141). Cells were seeded at a density of 25K cells/mL (2 mL/dish) and were allowed to adhere and reestablish for 18-24 hours before imaging. Cells were imaged using a Nikon Ti microscope equipped with a 10X phase contrast objective (Nikon Plan Fluor 10x/0.30 PH1 DL) and a Hamamatsu ORCA-Flash 4.0 V2 sCMOS camera. Environmental conditions were maintained at 37°C and 5% CO_2 using a Tokai Hit stage top incubator containing a 2-position insert for 35 mm dishes. To ensure consistent experimental conditions between the two groups of cells (PTEN and PTEN/MYO10), cells from each group were seeded and imaged in parallel using the 2-position insert. 5 randomized image fields for each dish were acquired every minute for 48 hours. The doubling time and mitotic duration of these phase contrast time-lapse images were determined manually using ImageJ (FIJI). The doubling time is defined as the number of frames (min) need for a newly divided cell to undergo a subsequent round of cell division. The mitotic duration is defined as the number of frames (min) from initial cell rounding to cytokinesis. All cell divisions and mitotic events from all 5 images fields from the respective cell groups were combined for the final population analysis. Experiments were conducted 3 separate times (n = 3).

Western blot analysis

Whole-cell lysates prepared from cells treated with vehicle or drugs were generated by incubating cell pellets in lysis buffer (50 mM Tris HCl at pH 7.40, 150 mM NaCl, 1 mM EDTA, 1.0% Nonidet P-40, and a mixture of protease and phosphatase inhibitors), on ice for 30 min. Cell debris was removed by centrifugation for 10 mins at high speed on table top centrifuge at 4^{o}C. Cell extract proteins were determined by the Bradford method and were separated by SDS/PAGE [10-12% (vol/vol) acrylamide] and transferred to polyvinylidene difluoride membranes. The membranes were blocked in 5% non-fat dry milk in TBST (TBS in 0.1% Tween 20) for 1 hr and then incubated with primary antibody in blocking solution for 2 hr, followed by incubation with secondary antibody in blocking solution for 1 hour at room temperature, and developed by using the enhanced chemiluminescence solution.

Orthotopic Tumor Implantation and Bioluminescence Monitoring of Tumor Growth

Intracranial tumor implantation was performed on 8 week post-natal female NOD-SCID mice obtained from Jackson laboratory (stock #005557). Under isoflurane-induced anesthesia, 50,000 luciferase expressing PTEN deleted and PTEN/Myosin 10 co-deleted murine GBM cells were injected in 2µL of culture media at coordinates X=1.5mm, Y=1.5mm and Z=2.5mm relative to the bregma. Tumor formation was monitored by intraperitoneal injection of 3 mg/kg body weight of D-luciferin (Xenolight D-Luciferin firefly potassium salt, PerkinElmer, catalog# 122799) in sterile phosphate buffered saline (PBS) followed by IVIS imaging. Once photon counts reached between 2.5-5.0 x 10^7/sec, animals were divided into two groups, with one group intraperitoneally injected with vehicle and other injected with 25mg/kg body weight of PARP inhibitor niraparib (Selleck, cat #S7625) 5 days/week. IVIS imaging was performed every 3-4 days and photon flux was calculated from the resulting signal.

Macropinocytosis assay

To investigate the effect of MYO10 deletion on endocytosis in GBM cells we used pHrodo Red dextran (Thermo Fisher Scientific, cat #P10361), which is non-fluorescent in solution but becomes fluorescent when internalized in endosomes. PTEN-deleted and PTEN/MYO10 co-deleted cells were plated on fibronectin coated chamber slides. After 24 hrs, cells were treated with 50µg/ml of pHrodo Red dextran and were fixed with 4% paraformaldehyde at 6, 12, and 24 hours post treatment. In some experiments, cells were pretreated with 200nM of dorsomorphin for 2 hr to inhibit AMPK signaling and then 50µg/ml of pHrodo Red dextran was added followed by incubation for 12 hours, followed in turn by fixation with 4% paraformaldehyde. Cells were counter-stained with DAPI and imaged for DAPI and dextran conjugate (with excitation/emission: 565/585) using Zeiss Confocal microscopy. Quantitated fluorescence intensity was normalized by dividing with the total number of DAPI-stained nuclei.

Atomic force microscopy

AFM experiments employed Dimension Fastscan with ScanAsyst™ and ICON head (purchased from Bruker Corp, Santa Barbara, CA). To study the cellular nanomechanical properties, we used an LC-CAL-A probe consisting of spherical tip geometry. The probe nominal spring constant (k) and the tip radius values were 0.1 N/m and 20 nm, respectively with the 38 KHz resonant frequency, making it suitable for soft cell samples. Before each experiment, the laser was aligned on the tip to accurately sense deflections in the cantilever. The tip was calibrated in media fluid surrounding the cells to account for changes in probe parameters due to hydrodynamic resistance by ramping on a hard surface (plain 60 mm culture dish containing Milli-Q water). The calibrated values for the probe were k = 0.01 N/m with deflection sensitivity of 30.7 nm/V and peak force tapping amplitude sensitivity of 804.9 nm/V at 1 KHz tapping frequency. The peak force amplitude was set to 300 nm for accurate tip-sample interaction. Cells were identified using an optical microscope attached to the ICON head and nanoindentation was performed at three regions of dimension 500 x 50 nm^2 as we have previously described (Kulkarmi *et al.,* 2019). Force-separation (F-S) curves generated from the interaction between AFM tip and sample were further analyzed. This technique solely relies on deflection in the cantilever as a result of various forces participating during the tip-sample interaction (Carvalho and Santos, 2012). Ramping parameters involved in nanoindentation technique were optimized as per our previous studies (Kulkarmi et al., 2019). For this study, the ramp size was 4µm, the ramp rate was 1 Hz with 2048 samples/ramp and the applied trigger threshold was 100 pN. For each dynamic time point, at least 14 cells were used with each cell indented no less than 10 times over a 500x50 nm^2 region yielding a minimum of 140 F-S curves. All experiments were performed at 37°C using a heated stage monitored closely by a temperature controller (Lake Shore Cryotronics, Inc, Westerville, OH).

Each ramp resulted in an F-S curve from which measures of stiffness, deformation and probe adhesion were extracted. However, these F-S curves had to be initially pre-processed followed by analyzing them using Bruker's Nanoscope analysis v1.9 software. Briefly, each F-S curve was subjected to boxcar filter to reduce the overall noise followed by baseline correction. As the indentation in the cell membrane was comparable to the tip dimension, a Hertzian contact model was employed by fitting the retrace curve to yield cell membrane stiffness.

$$F = \left(\frac{4}{3}\right)\left(\frac{E}{1-\vartheta^2}\right) R^{\frac{3}{2}} \delta^{\frac{1}{2}}$$

Where, F = Applied force, E = Young's modulus (stiffness parameter), ϑ = Poisson's ratio (material property, for cell = 0.3) (Ebenstein *et al.,* 2009), R = tip radius, δ = indentation of tip into the cell surface. Other nanomechanical properties such as deformation and adhesion were also obtained from the retrace curve for an acquired F-S curve. Origin Pro Lab software was used to calculate statistical significance and also to plot the data. Firstly, each dataset was first examined for normal distribution criteria and then One-way ANOVA test was applied to measure the significance. Statistical differences were determined to be significant at $p < 0.05$.

Statistical analysis

Statistical analyses were performed with Prism 8. Data are presented as means ± SD or SEM as noted in the text and figure legend. A two tailed t test was used to determine statistical significance (p values). Statistical significance was set at $p<0.05$. Error bars and n values of biological replicates for experiments are defined in the respective paragraphs and figure legends

Antibodies

Antibody	Vendor	Catalog #	Assay	Dilution
Myosin 10	Novus Biologicals	22430002	WB IHC IF	1:1000 1:200 1:800
HA	Sigma-Aldrich	11867423001	IHC	1:1000
Ki67	Vector	VP-K451	IHC	1:1000
γ-tubulin	Santa Cruz	sc-17787	IF	1:100
Pericentrin	Abcam	ab220784	IF	1:2000
Goat-anti Rabbit IgG Alexa 488	Molecular Probes	A32731	IF	1:500
Goat-anti Mouse IgG Alexa 594	Molecular Probes	A11005	IF	1:500
Phospho-Src (Tyr418)	Abcam	Ab4816	WB	1:500
Src	Cell Signaling	2108	WB	1:1000
Phospho-FAK (Tyr397)	Cell Signaling	3283	WB	1:500
FAK	Cell Signaling	3285	WB	1:1000
Phospho-Erk1/2	Cell Signaling	9102	WB	1:500
Erk1/2	Cell Signaling	4370	WB	1:1000
PARP	Cell Signaling	9532	WB	1:500
γH2Ax (Ser139)	Cell Signaling	9718	WB	1:1000
β-Actin	Cell Signaling	3700	WB	1:1000
Phospho-AMPK (Thr172,183)	Fisher Health Care	PIPA585649	WB	1:500
AMPK	Cell Signaling	2532	WB	1:1000
LKB1	Cell Signaling	3047	WB	1:1000
Phospho-Akt1 (Ser124)	Thermo Fisher	PA5-105161	WB	1:500
Akt1	Thermo Fisher	PA5-96351	WB	1:1000
Anti-GFP	Invitrogen	A11122	WB	1:1000